

Design, implementation, and performance of the primary reflector for SALTUS

Jonathan W. Arenberg^{a,*}, Leon K. Harding^a, Bob Chang^a, Steve Kuehn^a,
Dave Oberg^a, Michaela N. Villarreal^a, Arthur L. Palisoc^b,
Christopher K. Walker^c, Daewook Kim^c, Zach Lung^d, and Dave Lung^d

^aNorthrop Grumman, Dulles, Virginia, United States

^bL'Garde, Inc., Tustin, California, United States

^cUniversity of Arizona Department of Astronomy, Tucson, Arizona, United States

^dDA2 Ventures, Timnath, Colorado, United States

ABSTRACT. The Single Aperture Large Telescope for Universe Studies (SALTUS) is a mission concept for a far-infrared observatory developed under the recent Astrophysics Probe Explorer opportunity from the National Aeronautics and Space Administration. The enabling element of the program is a 14-m diameter inflatable primary mirror, *M1*. Due to its importance to SALTUS and potentially other space observatories, we focus entirely on *M1*. We present a historical overview of inflatable systems, illustrating that *M1* is the logical next step in the evolution of such systems. The process of design and manufacture is addressed. We examine how *M1* performs in its environment in terms of the operating temperature, interaction with the solar wind, and shape change due to non-penetrating particles. We investigate the longevity of the inflatable in detail, show that it meets mission lifetime requirements with ample margin, and discuss the development and testing to realize the flight *M1*.

© The Authors. Published by SPIE under a Creative Commons Attribution 4.0 International License. Distribution or reproduction of this work in whole or in part requires full attribution of the original publication, including its DOI. [DOI: [10.1117/1.JATIS.10.4.042306](https://doi.org/10.1117/1.JATIS.10.4.042306)]

Keywords: SALTUS; far-infrared; inflatable reflector; space telescope; space observatory

Paper 24073SS received May 24, 2024; revised Aug. 13, 2024; accepted Aug. 15, 2024; published Sep. 9, 2024.

1 Introduction

The Single Aperture Large Telescope for Universe Studies (SALTUS) is a mission concept developed for the ongoing National Aeronautics and Space Administration (NASA) Astrophysics Probe Explorer (APEX) opportunity. From the Latin for “leap” or “jump,” SALTUS is a far-infrared (far-IR) space observatory operating from a halo orbit around *L2*. SALTUS is capable of observing the first galaxies, protoplanetary disks at various evolutionary stages, and a wide variety of solar system objects, utilizing the large photon collecting power and angular resolution afforded by its 14-m diameter unobscured clear aperture and an operating wavelength ranging from 30 to 659 μm . The science program for this observatory is described at length in the other contributions in this special section.¹

The key enabling feature of the SALTUS architecture and the subject of this paper is its large aperture inflatable primary reflector known as *M1*. *M1* is connected to the spacecraft via a deployable ~ 17 -m single boom.² The lenticular reflector is shown in the context of the SALTUS mission in Fig. 1 and is constructed of a 0.5 mil (6.75 μm) thick polyimide film.

*Address all correspondence to Jonathan W. Arenberg, jon.arenberg@ngc.com

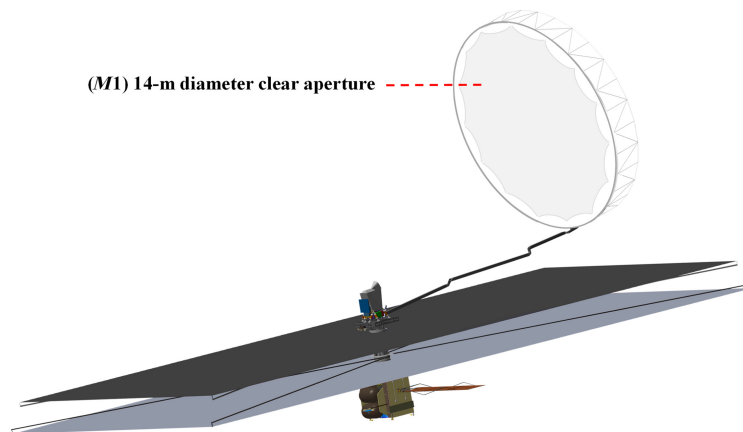


Fig. 1 3D rendered image of the SALTUS observatory, featuring an inflatable 14-m diameter off-axis primary mirror technology and its sunshield for radiative cooling below 45 K (image credit University of Arizona).

This paper is dedicated to addressing the most obvious questions surrounding such a large non-traditional optic. How is such a mirror designed and constructed? How can such a system maintain performance in the hostile environment of space? Furthermore, if such performance is established, how long can it be maintained? What are the plans for *M1*'s development and test?

The fundamental promise of an inflatable primary optic is the ability to enable very large collecting areas, such as for low mass, volume, cost, and schedule. The authors of this paper are some of the principals in a recent APEX proposal, SALTUS, which is based on this fundamental promise. The purpose of this paper is to document our recent advances in developing inflatable optics to increase confidence in their technical viability. We present our analysis as generally as possible, using the work we did for SALTUS to build upon the prior conceptual design of OASIS, an Astrophysics Medium Explorer proposal.³

The possibility of inflatable systems for applications in space is almost as old as the space age itself. In fact, one of the early demonstrations of the relevance of advanced space technology came with EchoStar and the first demonstration of advanced global communication and other early experiments.⁴⁻⁶ Inflatable systems have been studied for various applications, such as structures, reflectors, and even habitats.⁷⁻¹¹ There are also many examples of inflatable systems being considered the basis of space-based optical systems.^{7,9,11-13} To underscore the idea that inflatable optical systems are hardly a novel concept, consider the results of a literature search for inflatable reflectors and antennas for space, as shown in Fig. 2. The figure illustrates that this basic architecture has been investigated for over 40 years. These activities, particularly those concerned with making reflectors, were very active and well funded in the 1990s, with much of the art summarized in a book edited by Jenkins.⁵ The cessation of research following the 9/11 attack has left the development of inflatable systems largely stagnant. Since the 2000s, the literature on inflatable optic systems focused on the inflatable technology itself and not its integration into a full system. A NASA experiment in the late 1990s, the Inflatable Antenna Experiment, which is

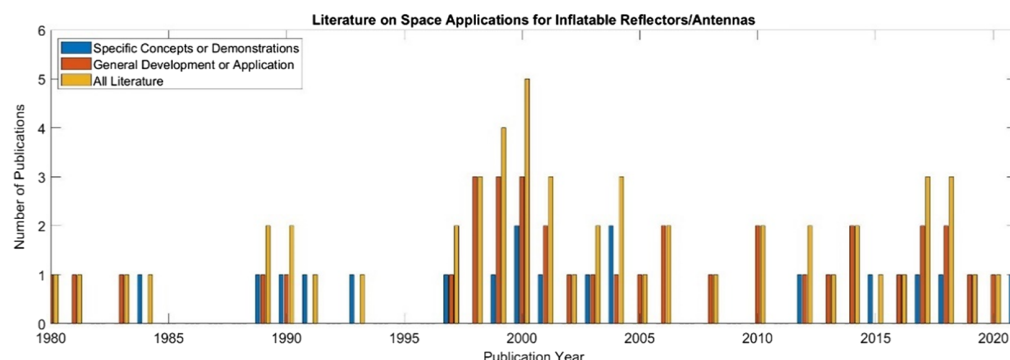


Fig. 2 Literature on inflatable space telescopes from the past 40 years.

a 14-m diameter parabolic reflector deployed from the space shuttle on Mission STS-77, has direct legacy to SALTUS as a proof of concept.¹⁴

Due to their lighter weight and more volumetrically efficient systems, inflatable optics are a natural next step in the evolution of space optics. This trend is founded on a fundamental truth of the physics of reflective optics; light from a cosmic target only interacts with the reflective coating. Anthropomorphizing a bit, the cosmic signal only “knows” the coating layers and their properties and does not “see” or interact with the substrate that holds the surface in place. What matters is configuring the reflective surface in the right shape and at the right place in a system to achieve and maintain performance. *M1* offers the possibility of creating and maintaining a very large aperture optical system, at low mass and volume, thereby enabling scientific discovery previously unimaginable.¹ This kind of promise seems almost too good to be true. To convince ourselves that this is not “21st-century optical snake oil,” we methodically analyzed many of the key questions associated with the realization of a large space aperture based on inflatable optics and present the results in this paper.

A completely comprehensive treatment of inflatable optics is well beyond the scope of a journal paper, such as this. We focus on those elements of the inflatable reflector that we believe show the viability of the technology and our implementation of it. The process of modeling an inflatable optic and the resulting optical design are separate reports.^{10,15,16} For a system as large as SALTUS, we need to show that it is possible to measure the primary aperture and to do so without recourse to a vacuum chamber.¹⁷ More details on other aspects of the SALTUS observatory architecture can be found elsewhere in this special issue.²

2 Design and Manufacturing of *M1* and Inflation Control System (ICS)

The primary mirror system consists of *M1* and the surrounding truss that holds the reflector in tension and serves as the primary mechanical interface between *M1* and the deployable boom. Both the boom and truss contain mechanisms to adjust and maintain alignment.

M1 is an off-axis parabolic-shaped inflatable formed by edge bonding two elliptical, 0.5 mil (12.67 μm) thick, diameter polymer films. *M1* has an optical clear aperture equivalent to a 14-m diameter, and the physical size of *M1* is larger, \sim 15-m diameter. The films are constructed from trapezoidal gore segments that are thermally formed on an aluminum mandrel to the proper figure, and they are edge bonded together in such a way that, when inflated, a seamless, off-axis parabolic shape is produced. *M1* is filled with far-IR spectrally inert and noble helium (He) and inflated to the design pressure, P_0 of \sim 5.1 Pa. When operating in a space environment, these pressures produce a wrinkle-free surface.^{16,18} The inflation pressure is actively controlled to ensure that the correct figure is maintained during science observations over the mission lifetime.

Both the design and verification of *M1* will be analytically based and validated on a subscale of 8 m and full flight size representative engineering models; see Sec. 4. To demonstrate that metrological data are sufficiently accurate to validate a finite element model (FEM), the SALTUS team carried out a series of measurements on an existing 1-m diameter test article in a chamber at the Northrop Grumman Space Park Facility.^{10,16,17} This experimental series involved inflation with various gases at atmospheric pressure and vacuum to quantify gravitational and buoyant effects. Test measurements and analytical models indicate the shape difference in *M1* between being on-ground and on-orbit as gravitational effects will be only in low orders. The low-order shape errors of *M1* and the induced aberrations such as coma can be simply compensated by the rigid body motion of *M1* with respect to the corrector unit.¹⁵ The required rigid body motions are facilitated by actuators that are a typical element of our planned AstroMesh™ reflector system.²

The AstroMesh™ reflector was developed in 1990 and has been refined over the last 30 years with 13 successful mission deployments.^{2,18} A sketch of *M1* installed in a deployed AstroMesh™ is shown in Fig. 3. The deployed AstroMesh™ reflector structural integrity comes from three components: the perimeter truss, the net consisting of kevlar webs, and the tension ties. The net is necessary to give the deployed truss radial stiffness by reacting tension and compression loading in the webs. Without the net, the radial stiffness of the truss depends on the

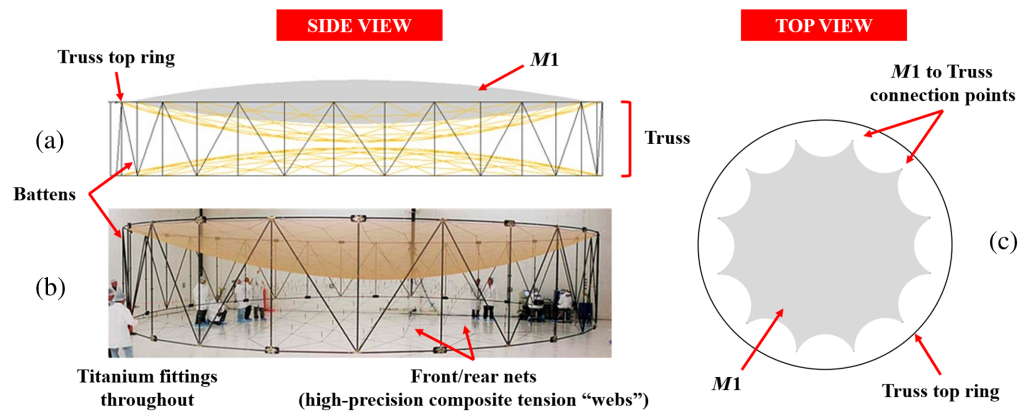


Fig. 3 AstroMesh™ truss and SALTUS reflector (a) shows a sketch of the M1 reflector located in the AstroMesh™, (b) Photograph of a typical AstroMesh™ truss, note the gold mesh and the size of the technicians, a key future trade will be to retain or remove the gold mesh as it contributes significantly to the stiffness of the deployed truss (c) shows a sketch of the M1 face on, the very small diameter ties are not resolvable at the scale of this drawing.

bending stiffness of the truss members. The tension ties preload the net, so it can react to compression loading.

2.1 M1 Design Process

To achieve the M1's desired parabolic shape, we first have to solve the inverse problem, that is, finding the shapes of the gores that give the final desired 3D surface shape when inflated. This inversion process has been coded into a computer program FLATE. Given a final shape, FLATE calculates the initial un-stressed shape of the membrane gores.¹⁹ Figure 4(a) illustrates the inverse problem, and Fig. 4(b) shows how membrane gores are joined together to form the parabolic reflector. A canopy [as shown in Fig. 4(c)] is used to create a lenticular volume to contain the inflation pressure.

Utilizing the SALTUS optical design, Kim et al.¹⁵ showed that the millimeter-level surface figure deviations across the M1 aperture can be corrected to provide a diffraction-limited performance in the far-IR. Surface accuracies on the order of 0.5- to 1-mm root mean square (rms) have been measured on reflectors up to 3 m in diameter. The 14-m diameter inflatable antenna experiment (IAE) reflector had a measured accuracy of 2-mm rms overall, with one 3-m section having an error of 0.365-mm rms.¹⁴ With the most recent fabrication method using very precise proprietary tooling and a mandrel design, we expect surface accuracies of less than 1-mm rms for diameters up to 30 m. We recently built and measured a 3-m diameter, $F/D = 1$ inflatable reflector to have a surface accuracy of $\varepsilon = 0.65 - \text{mm rms}$. This test article was built on existing mandrels. If the 3-m test article is built using the more precise fabrication mandrels planned for use on SALTUS, the surface accuracy will be higher.

2.1.1 Preliminary finite element analysis of SALTUS

Figure 5 shows the finite element model (FEM) mesh used by the FAIM code used to predict M1's shape.¹⁹ FAIM has been validated against known analytical solutions as well as

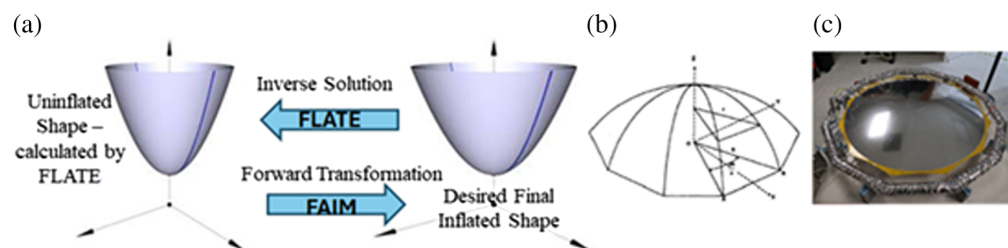


Fig. 4 (a) Solving the inverse problem. (b) Reflector made with pie shaped gores. (c) An inflatable reflector made with 24 aluminized Kapton gores (image credit L'Garde).

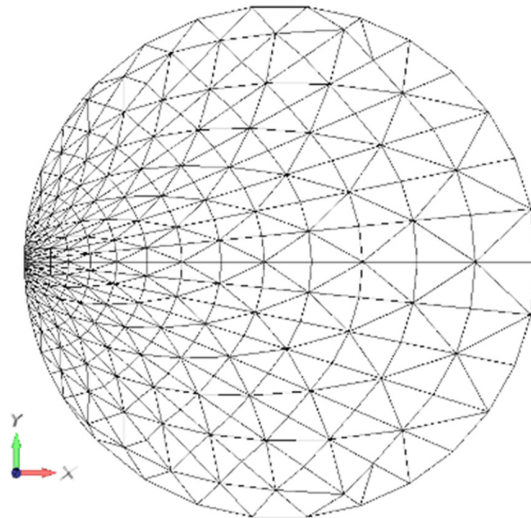


Fig. 5 Surface accuracy as a function of inflation pressure.

experimental results and showed excellent agreement.^{16,20} FAIM is a geometrically nonlinear finite element analyzer with membranes and tension-only cables in its element library. It can accept loadings of internal and external pressure, nodal forces, element forces, nodal/element temperatures, body acceleration, and pre-stress. Boundary condition inputs include zero and non-zero displacements, spring, and skew boundary conditions, where nodes are restrained to only move along a plane not parallel to the global $x - y$, $y - z$, and $x - z$ planes.

The SALTUS uninflated seamless shape is first calculated using the FLATE code and used to generate the geometry of the FEM. The inflation pressure was chosen to result in a film stress of $\tilde{6}.895$ MPa (1000 psi). The boundary condition at the perimeter of the reflector consists of displacements of the outer perimeter nodes to their final inflated $x - y - z$ location. Cable elements were used to simulate the effect of the seam tapes. The results of the FAIM run at varying pressures are summarized in Fig. 6. Figure 7 shows a zoomed-in view of the rms error near the minimum. The pressure corresponding to the minimum rms error, ~ 5.019 Pa, is P_0 , the nominal designed-for inflation pressure. The dashed vertical lines in Fig. 7 represent our initial inflation tolerance, $0.001 P_0$, which shows that this error in inflation is equivalent to an increased surface error of $11 \mu\text{m}$ rms of the pressure tolerance range. Figure 8 shows the change in focal length with $M1$ pressure.

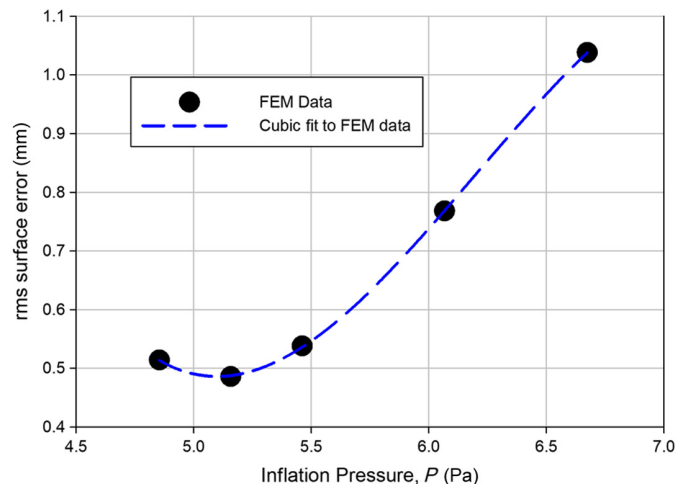


Fig. 6 Typical mesh for modeling (image credit L'Garde).

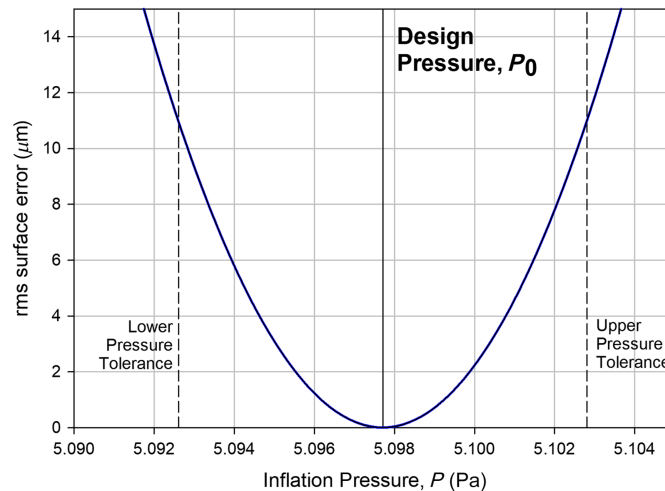


Fig. 7 Exploded view of rms surface versus pressure. The error is relative to the minimum surface error.

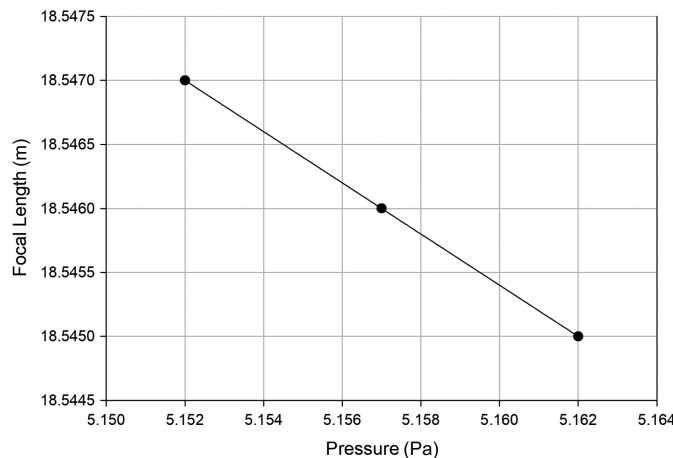


Fig. 8 Focal length as a function of inflation pressure.

2.1.2 Tolerances and shape budget

The sources of inflatable reflector surface errors come from manufacturing and environmental factors. These include tolerances in (a) gore shape, (b) mounting to the perimeter truss, (c) material property variation over the membrane continuum [modulus, coefficient of thermal expansion (CTE), thickness, etc.], (d) thermal effects on orbit, and (e) material creep under heightened stress and temperature.

The use of thermo-forming using highly accurate 3D gore mandrel assemblies reduces the gore shape error to its minimum, limited by the precision and accuracy of the mandrels, and it is expected to be independent of the optical form, on or off axis. The reduction of errors due to mating with the perimeter truss can be reduced using highly accurate fabrication support equipment.

SALTUS utilizes a sunshield and has a limited field of regard (FOR).² The range of expected temperature variation over the FOR is less than 1K (hot to cold) and is discussed in Sec. 3.4.3. This small temperature change makes the attitude-dependent thermal distortion small.

The mean operating temperature of the inflatable SALTUS reflector is ~ 37 K, rendering the effect of material creep and its impact on shape distortion to a minimum.¹⁹

The nominal membrane film stress on the inflatable SALTUS reflector is 1000 psi, which makes *M1* unwrinkled and, at least piecewise, a smooth and continuous surface. We also carried out measurements of the roughness of likely membrane materials for their suitability as specular reflectors, also known as good mirrors.²¹ In Ref. 21, we find that the measured roughness of a typical membrane with coating is ~ 0.05 μm rms. Using the conventional approximation, the total

integrated scatter from a surface at a reference wavelength of $30\ \mu\text{m}$ is ~ 0.00044 . Thus, the scattered energy is a very small fraction compared with the specular reflection energy, which is 1 to 0.00044. Thus, we can confidently claim that the *M1* surface is specular, which has been confirmed experimentally.¹⁷

2.2 Optical Prescription and Performance

The on-orbit performance of *M1* is predicted using a validated FEM. Model validation will come from measuring the surface shape of the inflatable reflector on the ground as a function of the inflation pressure, temperature, temperature variation over the surface, and boundary conditions. See Sec. 4 for more details on the test and development plans.

2.3 Manufacturing

The SALTUS *M1* builds on the legacy of the 14-m diameter inflatable antenna experiment (IAE) L'Garde built for NASA flown on the Space Shuttle Mission STS-77 in May 1996.¹⁴

The SALTUS baseline calls for clear 0.5-mil-thick polyimide and 0.5-mil-thick aluminized polyimide for the canopy and reflector, respectively. These materials were chosen because they have high transmittance at the wavelength of interest for the specific science and are tolerant to the environment.^{22,23} These baseline materials are similar to those chosen for the JWST sunshield.²⁴ Material choices, i.e., specific polymers to use for flight, will be studied and refined further as we proceed with the development.

The flight material membrane must meet a wide range of requirements that are yet to be fully defined, such as micrometeoroid impact robustness, electrical conductivity, coefficient of moisture, thermal expansion, thickness uniformity, radiation, and ultra-violet damage resistance. Detailing these requirements and conducting the qualification plan are activities that will be conducted early in the program, very similar to the TRL-6 program carried out on the sunshield layers for the Webb Telescope at Northrop Grumman in the middle 2000s.²⁵

As discussed in Sec. 2.1, the attainment of an accurate reflector surface starts with accurately shaped gores, the shape of which is derived from the FLATE calculation of the initial uninflated shape. The desired high accuracy will not be achieved if the gores cannot be seamed together with the required precision. The seaming of all gores for both the canopy and reflector is followed by an acceptance measurement prior to bonding the perimeter doubler around the lenticular. An example of the (scalloped) perimeter edge support for an inflatable lenticular is shown in Fig. 9.

2.3.1 Assembly, integration, and measurement

Each gore of the 14-m diameter SALTUS *M1* will be thermo-formed using a proprietary process. It uses a highly accurate 3D gore mandrel assembly. An example of a thermo-formed Kapton membrane is shown in Fig. 10.²⁶ It is noted here that the curvature of the membrane shown in Fig. 10 is more severe than the curvature of the 14-m diameter SALTUS *M1*.

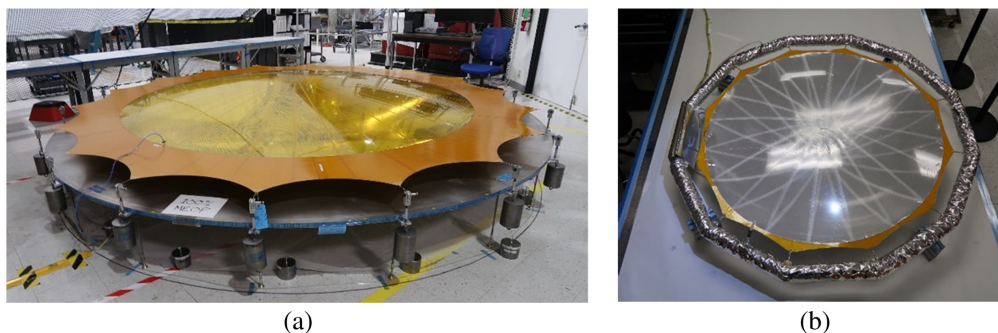


Fig. 9 (a) 3-m diameter inflatable lenticular showing its scalloped perimeter doubler edge support. (b) Fully inflated 1-m diameter lenticular with inflatable torus support, diameter inflatable solar concentrator built by L'Garde for TransAstra Corporation in support of their *in situ* resource utilization activities (image credit L'Garde).

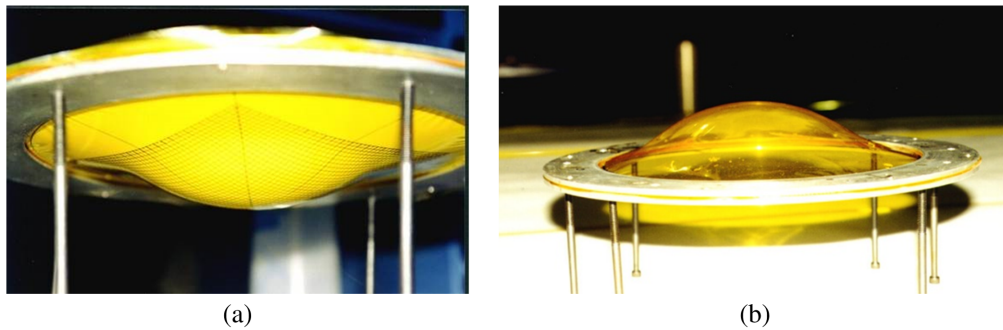


Fig. 10 Thermo-formed Kapton membrane (image credit L'Garde). (a) Membrane and support equipment prior to thermo-forming, (b) final thermo-formed membrane with the support equipment removed.

Figure 11 shows the gores of the 3-m diameter. These gores were made from flat gore segments (not thermo-formed); the surface figure accuracy obtained for the fully assembled 3-m on-axis reflector is $\varepsilon = 0.65$ -mm rms, which shows the robustness of the L'Garde code used. The use of a thermo-formed initial uninflated configuration for SALTUS will only enable higher surface accuracy.

We designed, fabricated, and measured antenna reflector diameters ranging from $\frac{1}{2}$ to 1,²⁷ 3,²⁸ 7,²⁹ and 14 m.³⁰ The 7-m reflector is shown in Fig. 12(a), and the 14-m IAE reflector on-orbit is shown in Fig. 12(b).

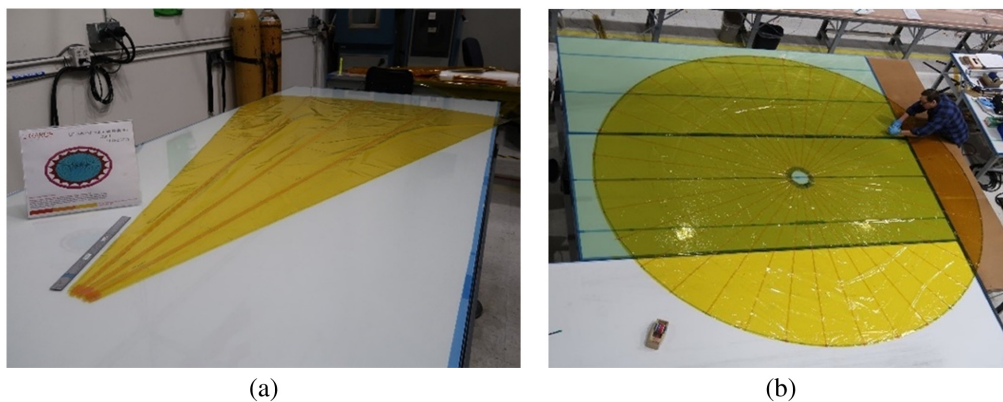


Fig. 11 3-m diameter gores laid out and bonded (image credit L'Garde).

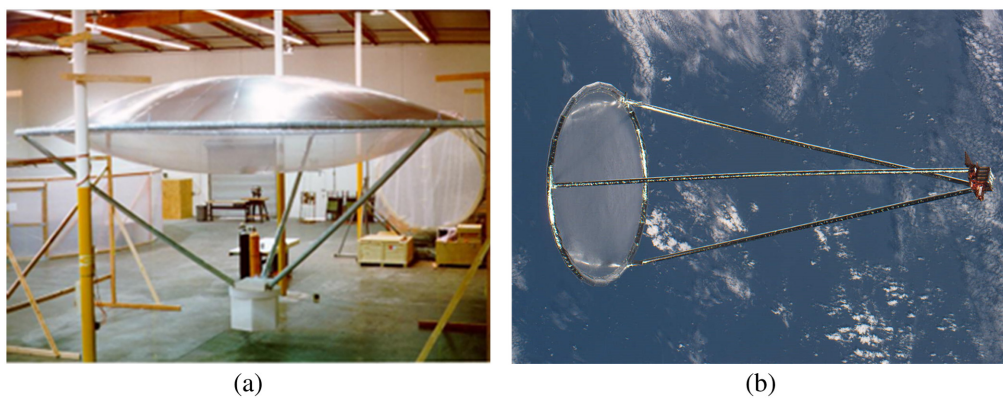


Fig. 12 (a) 7-m diameter, $F/D = 0.5$ On-Axis Reflector Canopy. (b) IAE on orbit. [Panel (a) image credit L'Garde; panel (b) image credit NASA].

2.4 Expected Performance

The presence of localized deviations due to the sealing lines has been reduced by several means. In the design of the gores, we analytically consider the presence of thicker seam tapes at the sealing line areas in our calculation of the gore shape of the initial uninflated configuration. This means that, on inflation to the desired pressure, P_0 , we obtain a surface figure very close to that desired—in this case, a paraboloid. By design, the inflation pressure value is high enough to give membrane strains that remove the packaging wrinkles and creases. Reflectors designed in this manner and made by L'Garde show no visible distortions at the seams nor at the perimeter. This was the case on the 14-m diameter IAE as well as subsequent inflatable paraboloid reflectors. More recently, the 3- and 1-m diameter inflatable paraboloid reflectors that we designed and fabricated show the same wrinkle-free behavior.

SALTUS will use a highly accurate 3D Gore Mandrel Assembly that can thermoform the initial uninflated gore shapes, rendering them with curvatures not only along the meridian but also along the hoop direction. The use of thermoforming results in the uninflated shape of $M1$ being very close to the theoretical starting configuration and in continuous optical surfaces across sealing lines. Moreover, to make the initial shape even closer to the theoretical curvature, we use a “seamless approach” in conjunction with thermo-formed gores. Seamlessness is achieved using two sets of identical gores that are bonded in a staggered manner. The thermoforming of $M1$ gores results in the minimization of membrane thickness variation over the $M1$ surface.

Optical simulations of the SALTUS optical system show that the 7 mm of rms deviation from the best-fit-surface is correctible.¹⁵ The inflatable reflectors made to date, including the IAE, have surface accuracies better than this. Moreover, with our new fabrication method using the 3D gore mandrel assembly, we expect to achieve surface accuracies 5 to 10 times better than the current state of the art, which is below 1-mm rms. This combination of requirements and capabilities gives us confidence in our ability to build a successful SALTUS primary mirror, $M1$.

From the past L'Garde project called the “large inflatable structures,” analysis showed that, for a 21 K temperature gradient across the surface of a 15-m diameter reflector, the surface degradation is on the order of 2.5-mm rms. The low temperature and the low-temperature variation over the $M1$ surface can be known through analysis and experiments, and their deleterious effects on the $M1$ accuracy can be removed through design. The low-temperature gradients help to minimize the negative effects of the CTE and CTE non-uniformity over $M1$. There are also low CTE polyimides on the market that would be included in any selection process for the final flight materials.³¹

We performed experiments on subscale inflatables to determine the minimum film stress needed to remove wrinkles and creases due to packaging. The results of our experiments show that the film stress must at least be 4.5 MPa (650 psi). SALTUS's design pressure of 5.1 Pa results in a 6.89-MPa (1000 psi) film stress to assure that no packaging wrinkles and creases remain. Furthermore, we consider the creation of wrinkles and creases as we detail the stowing approach; see Fig. 13.³²

Measurements of the surface accuracy of inflatable paraboloid reflectors using Lidar and photogrammetry show that the surface accuracies achievable on SALTUS and IAE-like diameters are on the order of 1-mm rms. This was achieved after the reflector membrane was folded and packaged.

2.5 Stowage and Deployment

A concept for the packaging of $M1$ is depicted in Fig. 13. The outer annular ring in Fig. 13(a) is analogous to the scalloped perimeter doubler for the 3-m inflatable shown in Fig. 9(a). This doubler is folded, as shown in Figs. 13(a) and 13(b), and the canopy and reflector are suspended using fabrication support equipment, as shown in Fig. 13(c). After folding to the stowage size, the edges of the perimeter doubler are mated with the inner AstroMesh™ perimeter, followed by a “z-fold,” as shown in Fig. 13(c).

The deployment of the AstroMesh™ occurs first. Inflation of $M1$ to P_0 is initiated only after the perimeter truss is fully deployed and able to take load.

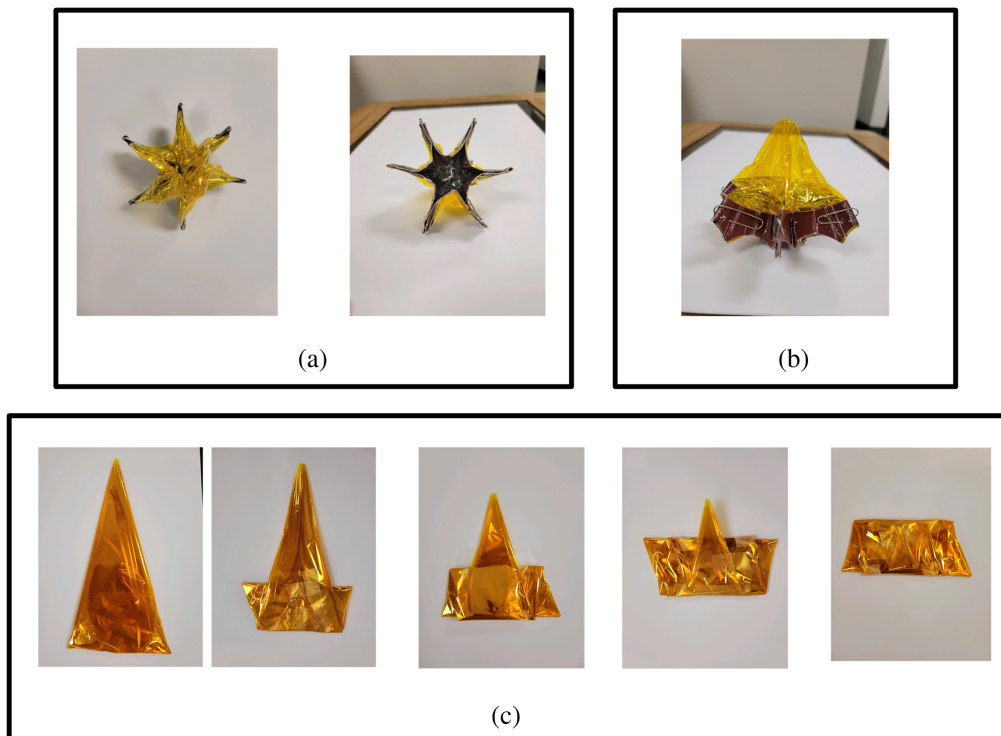


Fig. 13 Representation of the packaging of the inflatable lenticular. (a) Outer doubler shown (without inflatable). (b) Lenticular folded to the same diameter as available within the stowed AstroMesh truss. (c) The canopy and reflector are shown folded as cones with a projection on the plane that is similar to the opening of the central “hole” in panel (b). The reflector and canopy are then Z-folded as depicted in (d) blue and green (image credit L’Garde).

2.6 Contamination

Far-IR systems can be quite sensitive to contamination, especially if contamination increases the emissivity of a surface. In the case of *M1*, we must be concerned with contamination from the manufacturing process and ground handling as well as during flight. The main concern in flight will be particles and molecular contamination, mainly hydrocarbons and water from the inflatable tanks.

Figure 14 shows Q_{abs} , the dimensionless ratio of the physical absorption cross-section to the geometric area of the particle. Q_{abs} , calculated from Mie theory, is shown for particles of salt

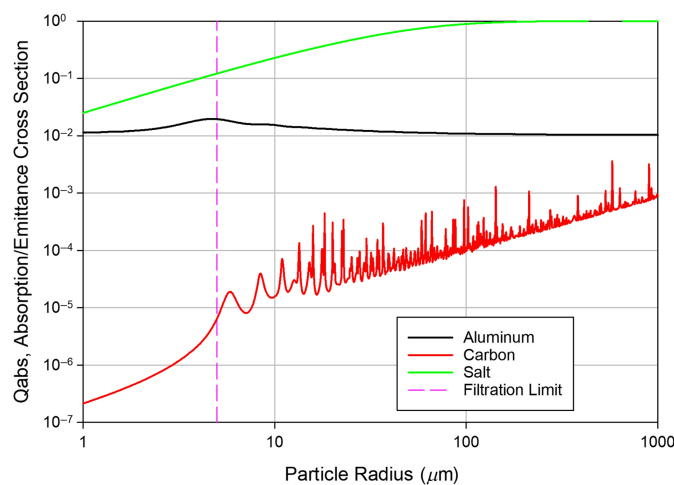


Fig. 14 Absorption cross-section, Q_{abs} , for candidate *M1* contaminant species, aluminum, carbon, and salt (NaCl).

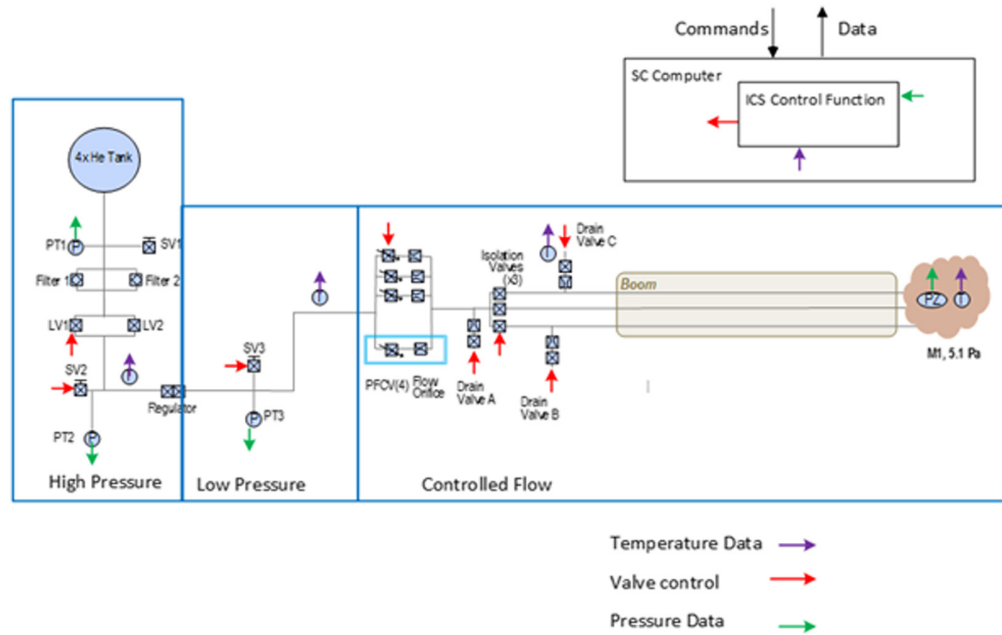


Fig. 15 Inflation control system block diagram.

(NaCl), carbon, and aluminum at a wavelength of $100 \mu\text{m}$ as a function of the particle size. The three chosen species are models for likely contaminants from the manufacturing process. Salt, NaCl, represents spit and sweat from human activity; carbon, C, is a surrogate for general soot and dust; and aluminum, Al, represents metallic debris. The emissivity of a particle is proportional to Q_{abs} and the fractional area coverage (FAC). As can be seen from the plot, the larger particles have larger absorption cross sections and therefore are the greatest potential contamination hazard in terms of emittance. We will manufacture *M1* in a clean environment and limit the particles that are on the membranes as it is assembled. Furthermore, techniques were developed to clean membranes of the size of *M1*, namely, the James Webb Space Telescope (JWST) sunshield layers, which had a measured coverage of 0.002 to 0.007 percent area coverage ($\text{PAC} = \text{FAC} \cdot 100$).³³ On this basis, we firmly believe that we can manufacture sufficiently clean membranes for *M1*.

It is well known in contamination control engineering that surface cleaning preferentially removes large particles, which is desired for this application.

To limit the particles inside *M1*, the ICS will use ultra-high purity He inflatant and will have a filter to limit particles from being pushed into the volume of *M1* over the life of the mission. This filter can be seen in the high-pressure section of the ICS block diagram (Fig. 15), limiting particle size to $\sim 5 \mu\text{m}$, indicated by the vertical red line in Fig. 14, and shows that the Q_{abs} will be limited to small values via the limitation of particle sizes.

Table 1 provides a summary of the impacts of contamination from all sources and the planned mitigation. In short, the contamination requirements and mitigations will ensure that the performance of *M1* is not compromised.

2.7 Inflation Control System (ICS) Architecture

The ICS is a closed-loop control system that regulates the flow of inflatant (helium) from high-pressure storage tanks on the spacecraft through gas lines on the boom to *M1*. It maintains the pressure within *M1* to meet the performance requirements over all attitudes and through the mission life during science operations. The ICS maintains reflector pressure during science observations within 0.001 of the design pressure, P_0 , namely, 5.1 mPa.

The pressure in *M1* is sensed through multiple strain gauges made from piezo-electric film bonded to *M1*, connected in a four-wire arrangement, and located outside the optical clear aperture. The strain gauge produces a voltage proportional to film strain, which is proportional to pressure and forms the basis of the error signal for the control loop. Our current baseline is to

Table 1 Contamination impacts and mitigations.

Contamination type (requirement)	Impact on SALTUS	Mitigation
Particulate (0.5 PAC/surface)	<ul style="list-style-type: none"> - Emissivity and scattering increase, transmission loss - Dominated by larger particles and those with sizes that are the same as SALTUS wavelengths³⁴ 	<ul style="list-style-type: none"> - <i>M1</i> is not cleanable after assembly, so it requires strict protocols for manufacture, storage, and monitoring - NB: Cleaning preferentially removes large particles, so the impact on the latter optics in the corrector module is very small¹⁵
Water ice (20 Å/surface)	<ul style="list-style-type: none"> - Transmission loss due to absorption loss mainly from 30 to 100 μm. 20 Å/surface is 1% peak loss ($\sim 45 \mu\text{m}$)³⁵ - Increased emittance in low emittance (coated) surfaces.³⁶ <p>This increase in emittance will be an increase in radiance for elements with limited sky view³⁷</p>	<ul style="list-style-type: none"> - Limit ice accumulation through design. Design sources, such as composite structures, to cool before optics or add heaters to optics. (Legacy JWST) Plan proper venting and contamination analysis to predict icing
Non-volatile residue (NVR) (30 Å/surface)	<ul style="list-style-type: none"> - Hydrocarbon layers from long-term exposure expected to be less than 10 Å.³⁸ Such a small layer at a reflecting surface has negligible optical impact^{33,36,37} 	<ul style="list-style-type: none"> - Flight hardware will be kept in a clean filtered environment

operate this loop as a bang–bang controller. Other control algorithms will be studied in phase A. Based on the error signal, gas will either flow into *M1* or be released from it.

The ICS architecture is presented in Fig. 15. The reservoir consists of four ARDE 4992 tanks, protected by Kevlar overwrap holding to 50 kg helium each at 4000 psia.² The latch valves, LV1 and LV2, are opened, and a regulator passes filtered helium to the low-pressure stage. This lower-pressure stage is plumbed to a series of proportional flow control valves (PFCVs) independently controlled using the three-channel spacecraft torque control resources and 12-bit regulated current source. The torque controller is a resource not needed by SALTUS because its orbit is an *L2* halo, well outside the Earth’s geo-magnetic field. Each PFCV is followed by a flow control orifice, which is sized to produce three channels with a dynamic range of ~ 6.46 , the dynamic range of the PCFV, with a 10% flow overlap, giving the ICS an overall dynamic range of ~ 218 . The upper mass flow rate is set by the maximum gas loss rate at EOL and, for the most demanding environment, ~ 0.9 mmol/s. The described arrangement gives a flow resolution of 6 nmol/s.

The ICS has four operating modes: (1) inflation, (2) discontinuous inflation, (3) continuous inflation, and (4) release. Mode 1, the inflation mode, is used after deployment of the boom and truss, where the inflation rate is slowly adjusted to the maximum rate and completes in ~ 40 h depending on the flight ambient temperature. The boom and truss are the first to deploy, and the sunshield layers are the last.² Mode 2, the discontinuous inflation mode, is required when the *M1* loss rate is below the minimum continuous flow rate of $\sim 3.7 \mu\text{mol/s}$. For the discontinuous inflation mode, a duplicate to the lowest flow channel is employed (indicated by a cyan box in Fig. 15), and a valve is opened for a fixed time (3 s) and then closed for an interval, which decreases as the *M1* loss rate increases with mission elapsed time. An additional valve is needed as the number of cycles for mode 2 is $\sim 70\%$ of the valve life as specified by the vendor. At ~ 9 to 12 weeks, the expected micrometeoroid (MM) flux will increase the loss rate to above the minimum continuous flow capability of the ICS. After the mean gas loss rate is above the ICS minimum continuous flow capability, the ICS will transition to mode 3, continuous flow, and will remain in this mode for the rest of the mission. The ICS has sufficient resolution that the error between the continuous loss rate of *M1* and the discrete inflow rates has a mean error of a few nmol/s, allowing the ICS control loop to maintain pressure within requirements. The final mode, mode 4, release, is needed when SALTUS changes attitudes resulting in an increase in *M1*’s temperature. The temperature change is proportional to the difference in the fourth root of

the cosine from the cold to hot pointing causing a pressure in excess of tolerance of 5.1 mPa. Excess inflatant is vented by opening the (redundant) drain valves (C or D); see Fig. 15. The vent diameter is sized such that the maximum release time is 20 min and will occur during slews. In a later more detailed design phase of the program, the vent diameter will be optimized to match the final slew rate of SALTUS so as not to impact observational efficiency.² The venting resulting from cold to hot point is discussed in more detail in Sec. 3.4.3.

3 M1 in the Operating Environment

SALTUS will operate in a halo orbit near Sun-Earth $L2$.² The SALTUS environment for our purposes is interplanetary space, where the main environmental challenges come from solar radiation, wind, and micrometeoroids (MMs). This section begins with a discussion of how we modeled $M1$'s temperature and concludes with a discussion of the impact of solar light pressure, solar wind and MM on the shape of $M1$, including the wounds caused by MMs' impacts. To determine if the effect is small, we consider a simple bound, limiting case. If the impact is larger than the tolerance, then the $M1$ design must respond. This response can be either a design feature to mitigate the impact or some other process to reduce the risk of impact. This process has been applied in the analysis of other high-performance systems.³⁰

3.1 Thermal Modeling of M1

$M1$ is essentially completely isolated in the sense of thermal conductivity. Furthermore, $M1$ has a very low mass and therefore, in effect, has no thermal transient, so we do not need to worry about transient analysis. The temperature of $M1$ is dependent on the temperature of the top layer of the sunshield and can be determined almost exactly from the Planck function and a little geometry. We seek a simple form to understand the drivers of the temperature of $M1$. As a first-order approximation, we consider $M1$ enclosed by a sphere; this sphere has two sections: the top hemisphere that is open and exposed to cold (4 K) space and the bottom hemisphere that sees the top layer ($L2$) of the sunshield. Let F represent the fraction of the full solid angle subtended from $M1$ by the sunshield; in this representation, $1-F$ is the fraction of the solid angle of cold (4K) space that $M1$ sees.

We want to know what the $M1$ mirror temperature, T_{M1} , is as a function of the temperature of the sunshield layer 2 (top or coldest layer), T_{L2} ; shield and mirror emissivities, ϵ_{L2} and ϵ_{M1} , respectively; and F . As $M1$ is conductively isolated and the system is in equilibrium, we know that

$$\text{heat in} = \text{heat out.} \quad (1)$$

The equilibrium condition in Eq. (1) is written as

$$A_{M1}\alpha_{M1}(F\epsilon_{L2}\sigma T_{L2}^4) = A_{M1}\epsilon_{M1}\sigma T_{M1}^4(1-F), \quad (2)$$

where A_{M1} is the area of $M1$, α_{M1} is the absorptance of $M1$, and ϵ_{L2} and ϵ_{M1} are the emissivities of the sunshield layer 2 and $M1$, respectively. Cancelling like terms in Eq. (2) gives

$$\alpha_{M1}(F\epsilon_{L2}\sigma T_{L2}^4) = \epsilon_{M1}\sigma T_{M1}^4(1-F). \quad (3)$$

Solving Eq. (3) for T_{M1} gives

$$T_{M1} = T_s \sqrt[4]{\left(\frac{\alpha_{M1}}{\epsilon_{M1}}\right)\epsilon_{L2}\left(\frac{F}{1-F}\right)}. \quad (4)$$

For this simple analysis, we use the so-called gray approximation, namely, $\alpha_{M1} = \epsilon_{M1}$. Under this approximation, Eq. (4) becomes

$$T_{M1} = T_s \sqrt[4]{\epsilon_{L2}\left(\frac{F}{1-F}\right)}. \quad (5)$$

In Fig. 16, Eq. (5) is solved for ϵ_{L2} in the (T_s, F) plane for various values of ϵ_{L2} when T_{M1} is 40 K. For the current baseline of SALTUS, $F \sim 0.1$ and T_{L2} has a maximum temperature of

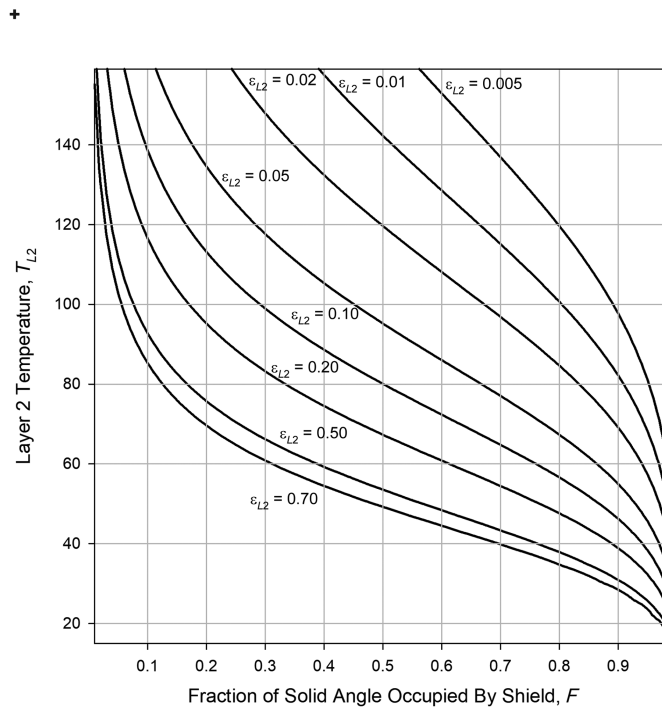


Fig. 16 Contours of layer 2 emissivity giving $T_{M1} = 45$ K as determined by Eq. (5).

~80 K; this design point is on the left of all contours, meaning that the emissivity of 0.7, that of a black membrane, results in an acceptable $M1$ temperature.

The results in Fig. 16 illustrate the wide range of possible successful architectures for SALTUS. The flexibility in the fundamental thermal architecture gives us confidence that, as the concept matures, we will continue to meet and perhaps exceed temperature requirements and deliver even greater sensitivity for the SALTUS mission.

We subsequently built a more traditional thermal model, which produced the $M1$ temperature shown in Fig. 17. For this model, the emissivity of the reflective surface is 0.015, and that of

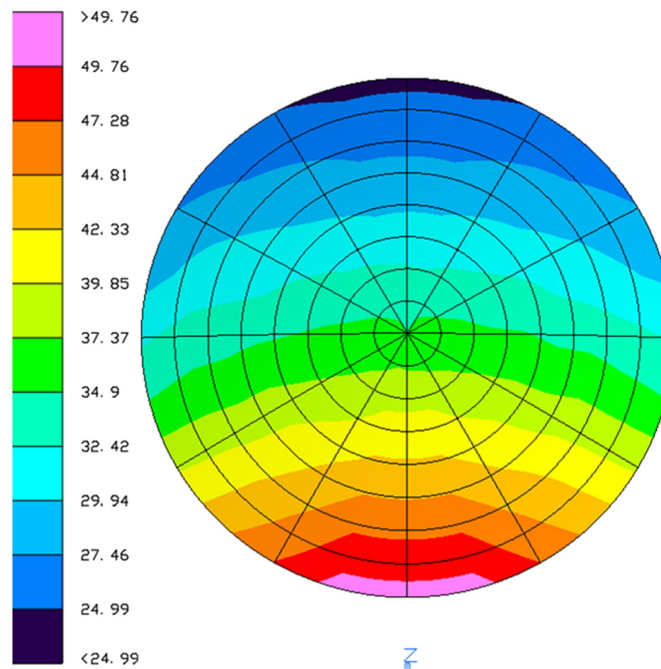


Fig. 17 $M1$ thermal map for SALTUS baseline design.

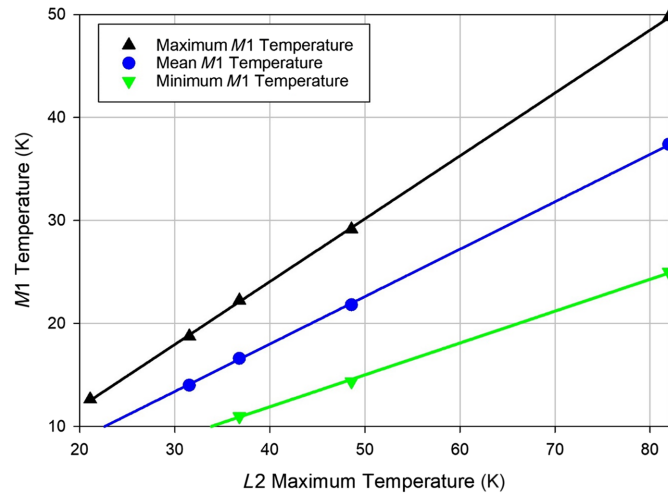


Fig. 18 *M1* temperature change in the *L2* environment.

the black backside is 0.6. In addition to the proposed baseline architecture, four other model cases were also run. For each of these cases, the maximum, minimum, and mean *M1* temperatures were determined and plotted against the maximum temperature of sunshield layer 2. These results are plotted in Fig. 18, and these data fall nicely on straight lines, verifying the results given in Eq. (5).

3.2 Interaction with Solar Emission

Photons and plasma from the Sun could pose a problem to *M1* in two ways. The first is by applying external pressure on the inflatable. The second is the accumulation of charge on *M1*'s surface that could result in electrostatic discharge that damages the observatory.

Pressure on *M1* can come from two sources, pressure from the solar wind (the outflow of protons and electrons from the sun) and the pressure exerted by the Sun's light. For this bounding analysis, we neglect the presence of the SALTUS sunshield.

At the *L2* Lagrange point, SALTUS' operational milieu, *M1* is embedded in the supersonic solar wind, which is composed of roughly equal parts protons and electrons traveling radially outward from the Sun. The dynamic pressure of the solar wind on an obstacle is calculated as $p = m_p \rho V^2$, where m_p is the proton mass, ρ is the proton number density, and V is the solar wind bulk velocity. We use data from the WIND spacecraft, a solar wind monitor located at Sun-Earth *L1*, to estimate this effect on *M1*. We focus on data from the solar maximum during the year 2001 when extreme solar wind disturbances are most likely to occur. We find that the maximum solar wind dynamic pressure recorded by the spacecraft was $\tilde{5}00\text{nPa}$ or $0.5\ \mu\text{Pa}$, which corresponds to pressure three orders of magnitude below the pressure tolerance of *M1*, 5.1 mPa. Therefore, we conclude that solar wind dynamic pressure effects can be neglected.

Pressure induced by solar radiation is I/c , where I is the solar intensity of $\sim 1370\ \text{W/m}^2$ and c is the speed of light. This gives a peak pressure from solar radiation of $4.56\ \mu\text{N/m}^2$ or $4.56\ \mu\text{Pa}$, orders of magnitude smaller than the 5.1 mPa tolerance defined in Sec. 2.1.1. The effects of solar wind and light pressure were evaluated without considering the effect of the sunshield. The presence of the sunshield can only improve matters, and we need no requirements on the performance of the sunshield as a solar windbreaker as even the full wind impact is negligible.

M1 will be exposed to the solar wind regardless of the sunshield, and if proper design mitigations are not taken, the charge could accumulate and cause damage or performance degradation. Furthermore, the sunshield's shadow precludes sunlight from dissipating the charge build-up on *M1*.

The accumulation of charge could deform *M1* through Lorentz forces as *M1* moves through the Sun's electromagnetic field or damage *M1* through arcing. It may be possible to show that these effects are small, but such analysis is challenging and uncertain as the environment is not well known and such a difficult analysis could be a resource burden on the program.³⁰ Consequently, we will take active design measures to avoid the build-up of charge by employing

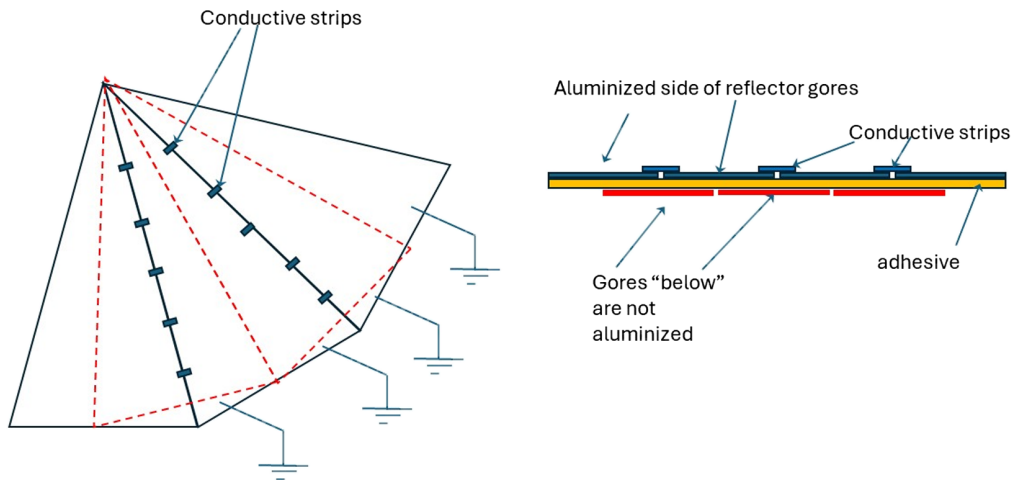


Fig. 19 Concept for grounding features incorporated along gore seams (image credit L'Garde).

dissipative coatings and connecting *M1* to the system ground. This global ground also avoids the risk of static charge build-up and the risk that such static cling will impede deployment. The current baseline calls for the incorporation of grounding features along seam lines. A conceptual sketch for our grounding scheme is shown in Fig. 19.

The grounding of a large membrane system has previously been implemented, with even more surface area than *M1*, namely, the JWST sunshield.²⁴ SALTUS will use similar design practices as JWST and apply any relevant lessons learned.

3.3 Micrometeoroids

MMs affect *M1* through two imperfectly known factors; the first is the environment or MM distribution at *L2*, and the second is the damage caused by the interaction of an MM of a given size and energy. The remainder of this section contains our work on understanding each of these factors and a discussion of the impact of potential gas leaks, critical time scales and inflatant longevity.

3.3.1 Micrometeoroid environment

MMs pose a threat to our inflatable primary reflector *M1* as the impacting particles will create punctures in the surface, resulting in gas loss. As the gas loss rate will partially determine the mission lifetime, it is crucial to properly estimate the impact rate at its *L2* Lagrange point location. One tool often applied for mission planning is SPENVIS,³⁹ which can provide the integral MM flux above a threshold mass. This model adopts an analytical description for the interplanetary MM flux near 1 AU from Grün et al.⁴⁰, which is valid for particle masses $10^{-18} < m < 1$ g.

It is important to note that this is a “sky-averaged” description of the integral flux. In their paper, Grün et al.⁴⁰ acknowledged that the sky-distribution is anisotropic and applied corrections to data taken from reference spacecraft, which pointed in directions of enhanced MM flux to arrive at this result. In this section, we compare the SPENVIS model with recent models and *in situ* data for expected fluxes at the *L2* location. In addition, we consider the pointing direction of *M1* in the context of current assumptions and derive a correction to the SPENVIS model for the SALTUS design.

Recent MM models rely on orbital elements of the parent body source to predict fluxes at specified solar system locations. Thorpe et al.⁴¹ considered contributions from Jupiter-family comets (JFC), Halley-type comets, Oort cloud comets, and asteroids. They developed an independent description for the sky-averaged integral flux at the *L1* location listed in their table 2.

In addition to the integral flux, Thorpe et al.⁴¹ also showed the predicted angular flux density from each population source for a momentum threshold of $\geq 1\mu\text{Ns}$, reproduced here as Fig. 20. These sky maps demonstrate that the various populations produce an anisotropic sky distribution, which has its largest concentrations in flux in the sunward and anti-sunward directions, with additional notable contributions in the north/south pole directions and near the prograde

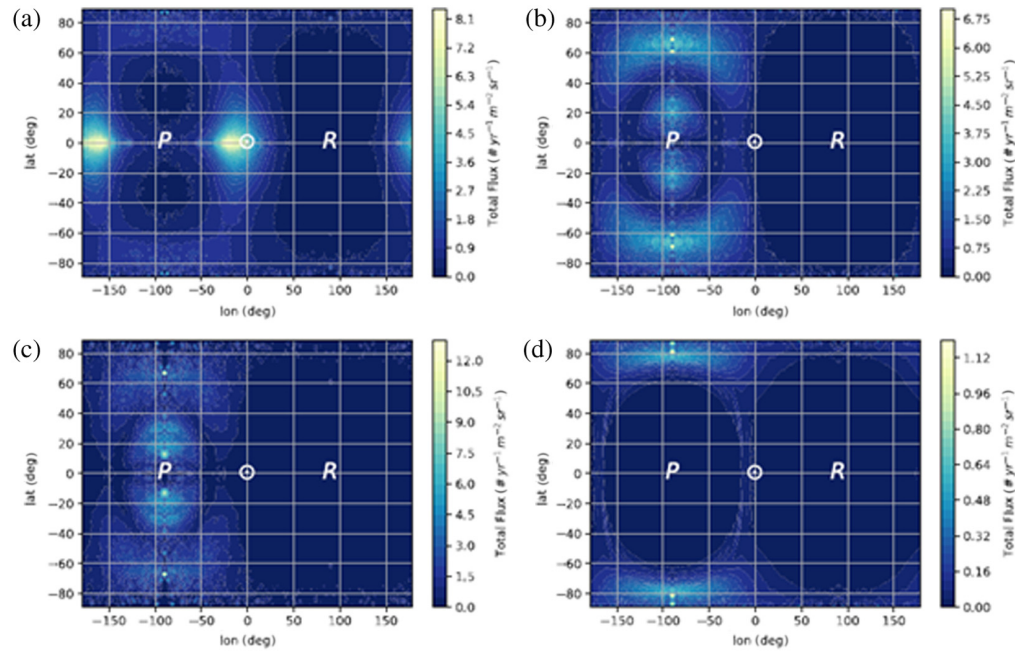


Fig. 20 Angular flux density by the parent body source for micrometeoroids with momenta $\geq 1 \mu\text{Ns}$. Maps are in a solar-orbital coordinate frame centered on a spacecraft located at $L1$, where the center circle denotes the subsolar direction, P is the prograde direction, and R is the retrograde direction. Jupiter-family comets are expected to account for $\sim 90\%$ of the micrometeoroid flux in the range considered, with this population flux primarily concentrated in the sunward and anti-sunward directions. (a) Jupiter-family comets (JFC). (b) Halley-type comets (HTC). (c) Oort cloud comets (OCC). (d) Asteroids (AST). This figure was reproduced with permission from Thorpe et al.⁴¹

direction. The sunward and anti-sunward fluxes are dominantly sourced from Jupiter-family comets (JFCs), which are expected to account for $\sim 90\%$ of the MM particles at $L1$ and similarly $L2$.⁴¹

In situ experiments have also been performed to track the rate of MM impacts on spacecraft. LISA Pathfinder was used as an omnidirectional detector of such impacts and found that the direction and frequency of sensed impacts were consistent with the sky distribution shown in Fig. 20.⁴¹ Similarly, a study was conducted for the Genesis spacecraft, which was at the $L1$ location for 2.33 years. This was based on an aluminum plate that pointed exclusively in the sunward direction.⁴² This study identified 32 confirmed impacts on a usable surface area of 220 cm^2 , with an additional 12 features classified as possible impacts.⁴²

To directly compare Thorpe et al.'s⁴¹ model with SPENVIS, we need to convert the integral flux from a function of momenta to one of mass. To do this, we use the momentum equation $p = mv$, where p is the particle's momentum, m is the particle mass, and v is the particle velocity. We assume a meteoroid speed of 35 km/s for all particle masses. Based on the momenta range for which these equations were derived, this would correspond to a threshold particle mass range of $\sim 3 \times 10^{-10} < m < 3 \times 10^{-4} \text{ g}$.

Fig. 21 shows a direct comparison of the sky-averaged integral flux of MM above a particle mass threshold (m) based on the SPENVIS model (blue line) and the Thorpe et al.⁴¹ model (red line). The figure shows that these models produce similar results for sky-averaged fluxes near $L1$ for masses $> 10^{-8} \text{ g}$.

We now consider deviations to the predicted $M1$ MM flux that may occur once the pointing direction is taken into account. The JFC MM sky distribution of an angular flux density is at the subsolar and antisolar points of $\sim 8 \text{ impactors}/(\text{m}^2 * \text{year} * \text{sr})$ for impactors with masses $> \sim 2.8 \times 10^{-8} \text{ g}$. The sky-averaged integral fluxes corresponding to this mass threshold predict 21.4 and 28.4 impactors/ $(\text{m}^2 * \text{year})$ from the SPENVIS and Thorpe models, respectively. We divide these values by the total field of view of the sky, $4\pi \text{ sr}$, to arrive at a sky-averaged angular

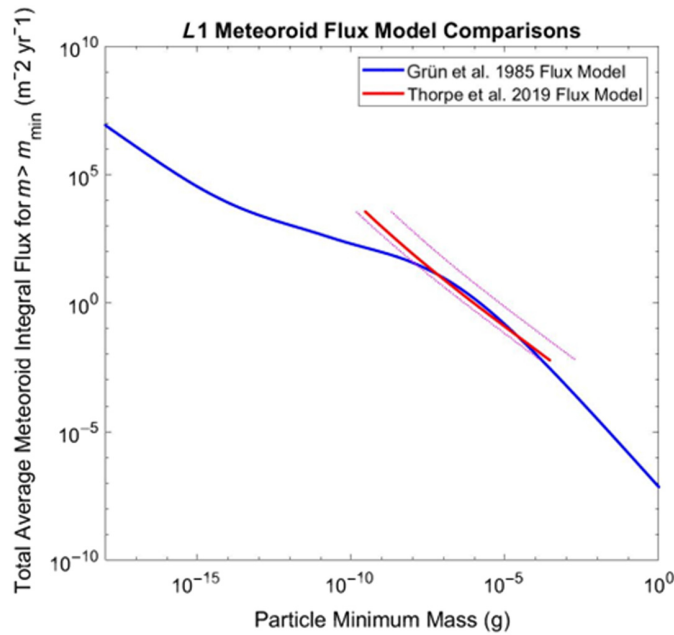


Fig. 21 Comparisons of the sky-averaged micrometeoroid integral flux above a particle mass threshold (m) predicted by SPENVIS (solid blue line) and Thorpe et al.⁴¹ (solid red line). The models produce similar results for threshold masses $> 10^{-8}$ g. The Thorpe et al.⁴¹ model is converted from a function of momenta to a function of mass assuming a particle velocity of 35 km/s. The dotted magenta lines show the bounds for particle velocities of $v = 5$ km/s and $v = 70$ km/s.

flux density for these models. This results in 1.71 and 2.26 impactors/ $(\text{m}^2 * \text{yr} * \text{sr})$ predicted from the SPENVIS and Thorpe models, respectively.

We also independently calculate a correction factor for the sunward direction by comparing predictions to the observed Genesis micrometeoroid impact counts. The detection method was sensitive to impacting particles with a size $> 1 \mu\text{m}$.⁴² Approximating the particle as a sphere with a radius of $1 \mu\text{m}$ and a density of 2.5 g/cm^3 (Ref. 40), this would correspond to a particle mass threshold of $m > 1.05 \times 10^{-11}$ g. This threshold is below the mass range valid for the Thorpe model and thus will only be compared with the SPENVIS prediction here.

The aluminum plate onboard Genesis was directed toward the Sun for the duration of the mission, with the plate shielded from 25% of the sky by other spacecraft structures.⁴² This would give a field of view for the plate of 1.5π sr. The sunward-directed angular flux density is calculated as

$$\begin{aligned} \text{Genesis Sunward Angular Flux Density} &= \frac{32 \text{ impactors}}{0.022 \text{ m}^2 * 2.33 \text{ years} * 1.5\pi \text{ sr}} \\ &= 132.5 \frac{\text{impactors}}{\text{m}^2 * \text{years} * \text{sr}} \end{aligned}$$

For a mass threshold of $m = 1 \times 10^{-11}$ g and dividing the sky-averaged integral flux by 4π sr, SPENVIS predicts an average angular flux density of 37.5 impactors/ $(\text{m}^2 * \text{year} * \text{sr})$, which is below the observed Genesis flux by a factor of ~ 3.5 . Thus, we find that the *in situ* data is in agreement with our analysis and that a correction factor in the range of 3.5 to 5 needs to be applied to the SPENVIS model to properly estimate fluxes on M1.

3.3.2 Interaction of M1 with micrometeoroids

Two things can happen when MM impacts an inflatable. The impactor can puncture M1 and cause loss, or it can fail to penetrate it and cause a mechanical disturbance.

The flux enhancement coming from the solar/antisolar directions is written relative to the standard Grün et al.⁴⁰ model as

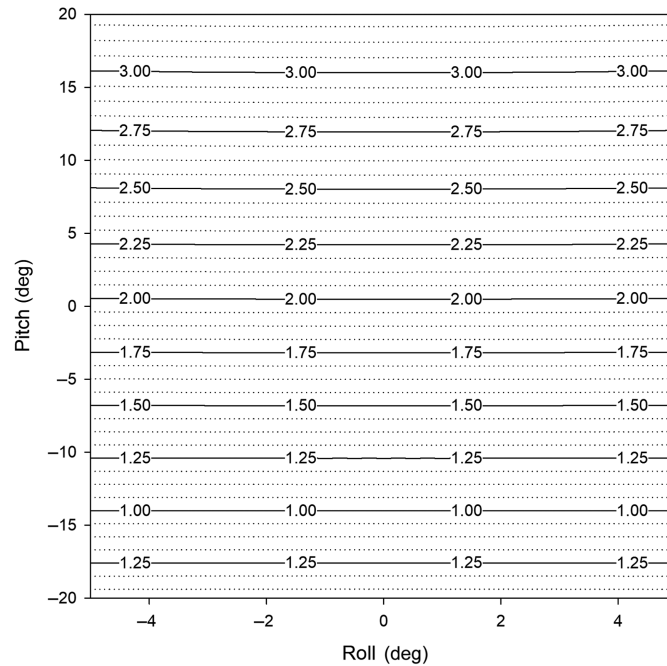


Fig. 22 $f(\theta)$ over SALTUS field of regard.

$$f(\theta) = f_0 + 4f_0 \cos \theta, \quad (6)$$

where f_0 represents the omnidirectional (background) flux. We can see from Eq. (6) that, when $\theta = 0$, the surface normal points in the solar direction and consequently the flux is enhanced by a factor of 5. However, when the surface normal points are perpendicular to the sunward direction, $\theta = 90$, the surface element is impacted only by the average background flux. To understand the flux variation of all combinations in between this range, we varied the solar pitch and solar yaw angles each over the SALTUS field of regard, and the results are presented in Fig. 22. We note here that this calculation was done assuming that the peak flux will be located at the subsolar and antisolar points. However, the incoming direction of the MM as seen from the body frame will be slightly off from the sun vector direction due to the motion of the spacecraft. This effect is similar to rain falling directly down on a car, but when viewed from the car frame, the rain appears to fall at an angle when the car is in motion. Future analysis will need to take into account the spacecraft velocity to more accurately calculate the flux enhancement at a given pitch and yaw.

Equipped with a description of the M1 MM environment and the enhancement factors, we can calculate the return period, the reciprocal of the rate, of particles impinging the surface. The rate of MM impacts on a telescope is estimated as

$$C = \varphi(m) f(\theta) \frac{\pi}{2} D_T^2, \quad (7)$$

where $\varphi(m)$ is the micrometeoroid flux and D_T is the telescope diameter. For SALTUS, the diameter of the primary reflector is 15 m, the MM flux, $\varphi(m)$, is represented by the Grün flux, and f is the model correction factor for non-isotropy of the flux.

We take the inverse of Eq. (7) to analyze the return period for impacts above a mass threshold size. The results of this calculation are shown in Fig. 23. Particles with $m < 10^{-8}$ g impacting may be problematic, depending on their effect on the telescope as they impact about once per hour.

3.3.3 Deformation of the surface

Now that we understand how often we anticipate impacts for any given size, we need to understand how these impacts may deform the surface. As M1 is inflatable, the deformation of the

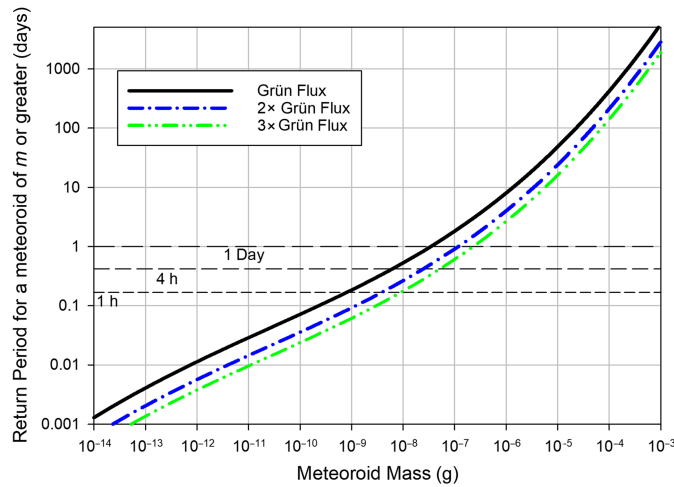


Fig. 23 Rate of micrometeoroid impacts above a given mass threshold, the isotropic Grün flux (solid black trace), 2× Grün flux (dash-dot blue trace), and 3× Grün flux (dash-dot-dot green trace).

surface will involve compression of the gas. We approximate the initial shape of $M1$ as a sphere. We treat the gas as ideal, assume that the temperature and number of moles remain constant during the interaction, and assume that all kinetic energy of the particle goes into compression of the gas as a bounding case. Figure 24 shows the kinetic energy of a particle with mass m striking $M1$ for various velocities. Equating the particle kinetic energy and the work done on the gas gives

$$\frac{1}{2}mv^2 = \int \vec{F} \cdot d\vec{l}. \quad (8)$$

The work done on a gas under isothermal conditions is expressed in terms of the volume change as

$$\int \vec{F} \cdot d\vec{l} = -nRT \ln\left(\frac{V_f}{V_i}\right), \quad (9)$$

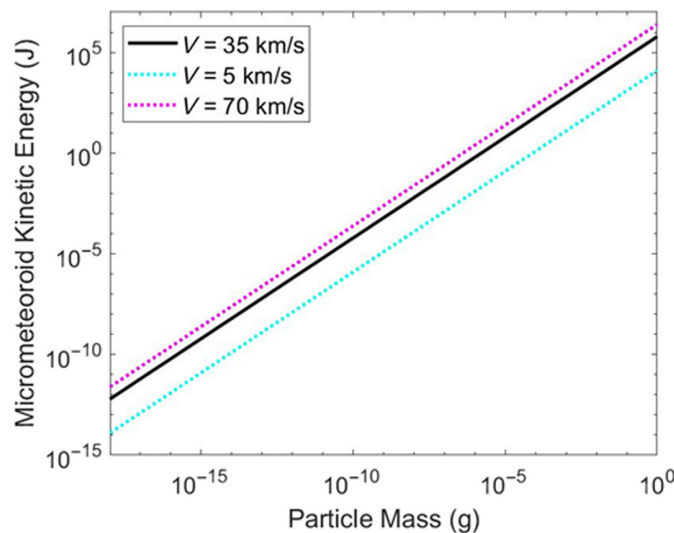


Fig. 24 Kinetic energy of micrometeoroids impacting $M1$. The black line depicts the chosen velocity of 35 km/s for all particle masses. The dotted cyan and magenta lines show the approximate upper and lower bounds of kinetic energy, respectively, for the full range of micrometeoroid velocities (5 to 70 km/s).

where n is the number of moles in the gas, R is the gas constant, T is the temperature of the gas, and V_f and V_i are the final and initial volumes of the gas, respectively. Substituting this into the previous equations results in

$$\frac{1}{2}mv^2 = -nRT \ln\left(\frac{V_f}{V_i}\right). \quad (10)$$

As we are interested in understanding the deformation of the $M1$ shape, we rearrange the above equation to solve for the final volume as

$$V_f = V_i e^{-mv^2/2nRT}. \quad (11)$$

We quantify the deformation in shape by calculating the change in radius due to the impact. The resulting radius after compression is

$$R_f = \left(\frac{3V_f}{4\pi}\right)^{1/3}. \quad (12)$$

For $M1$'s volume, $n = 1.6$ mols. Figure 25 shows the change in radius for an impactor with mass m and velocities of 35 (solid trace) and 70 (dashed traces) km/s. The three traces for each velocity correspond to different temperatures of $M1$. The horizontal dash-dot-dot trace is a change in the radius of a part in a thousand, our canonical tolerance. This can occur for particle masses greater than 10^{-7} g for $v = 70$ km/s and 10^{-6} for $v = 35$ km/s. From Fig. 23, we see that particles of this mass are expected less than once per day, even with directional enhancement, and should not have a significant impact on science operations.

We compare the radius displacement to the behavior of a spring to understand how the rigidity of $M1$ compares with other telescopes. We equate the work done on a spring to compress it a distance ΔR to the work done to compress the gas

$$\frac{1}{2}k(\Delta R)^2 = -nRT \ln\left(\frac{V_f}{V_i}\right), \quad (13)$$

where k corresponds to the spring stiffness. Solving the above equation for k gives

$$k = -\frac{2nRT}{(\Delta R)^2} \ln\left(\frac{V_f}{V_i}\right). \quad (14)$$

Figure 26 shows $M1$'s equivalent stiffness to different particle masses. For comparison, mirror elements of the JWST have a stiffness range of 10^5 - to 10^7 N/m. $M1$ exhibits a comparable stiffness for particles with masses up to 10^{-5} g, after which the effective spring constant is below the currently used telescopes.

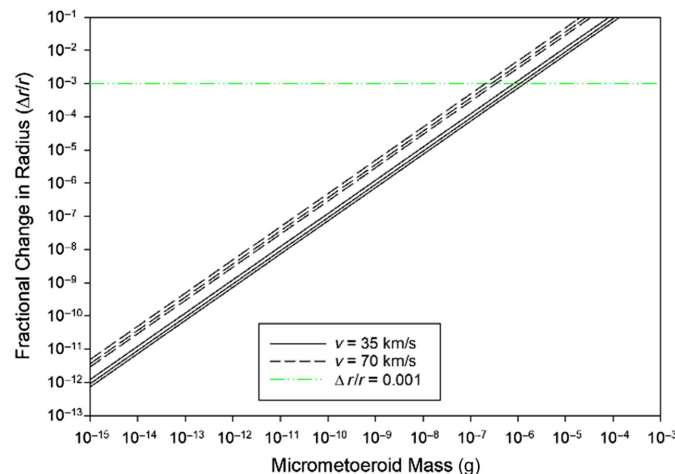


Fig. 25 Change in radius of $M1$ if all kinetic energy of an impacting particle goes into compressing the gas. Particle masses above 7×10^{-6} g change the radius by more than 0.1%.

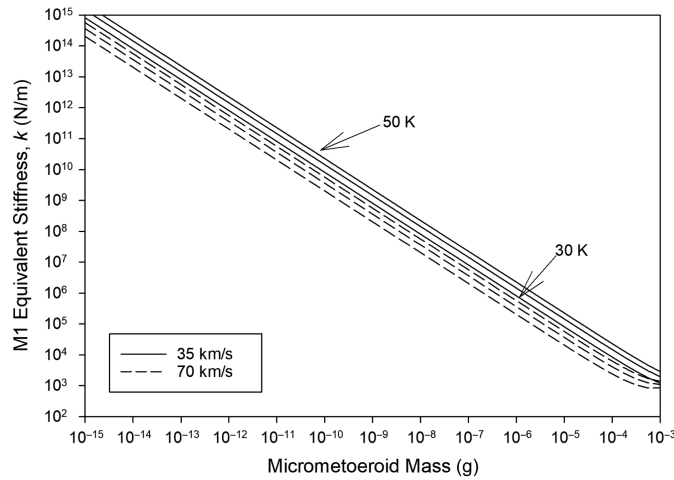


Fig. 26 Effective spring constant, k , if compression of $M1$ is modeled as a spring.

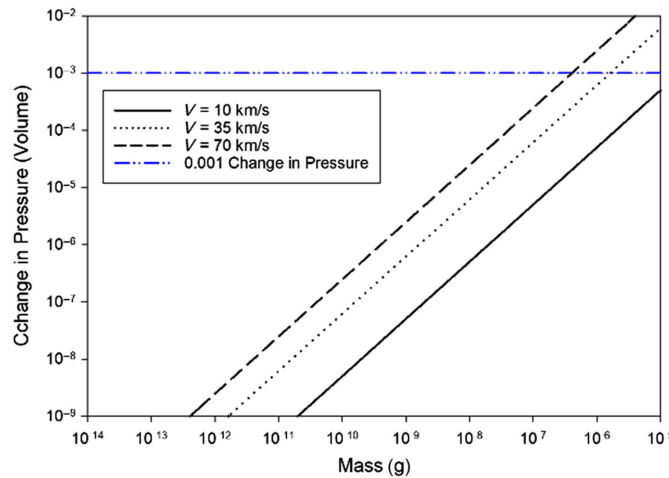


Fig. 27 Increase in pressure of $M1$ if the impacting particle's kinetic energy is assumed to go into compressing the gas. The red dotted line denotes the pressure tolerance of $M1$. This pressure tolerance is exceeded for particle masses greater than $\sim 10^{-5}$ g.

We also think about the compression effect in terms of pressure. As we set the number of moles and temperature to be constant, the final pressure is expressed as

$$P_f = \frac{P_i V_i}{V_f}. \quad (15)$$

Figure 27 shows the change in pressure due to a particle impact of a given mass. The red dotted line indicates the pressure tolerance of $M1$, $0.001 P_0$. The pressure tolerance is exceeded for particle masses $> 2 \times 10^{-6}$ g for $v = 70$ km/s and 8×10^{-5} g for $v = 35$ km/s; for these particles, the return periods are longer than a day, indicating no serious impact on the optical performance.

3.3.4 Optical impact of punctures from micrometeoroids

Section 3.3.3 describes potential disturbances to $M1$ from non-penetrating or elastic collisions. The current section deals with penetrating, non-elastic collisions that occur when the particle is above the ballistic limit. The aftermath of such collisions are wounds in $M1$. These wounds are interruptions in the optical surface and the inflatable gas containment; the former are optical imperfections, and the latter are sources of gas loss. Most of the impact holes are smaller than

the SALTUS operating wavelength and therefore will not impact optical performance in any significant way. The holes in the reflective surface appear as small reflective losses and look like particles obscuring the surface. At the end of life, this fractional area of the holes is $\sim 10^{-4}$, somewhere between MIL-STD-1246 Class 70 and 300, depending on slope, and is still a very clean optical surface in any regard.⁴³ The analysis of gas losses from these holes is given in Sec. 3.4.3.

3.4 Inflatant Longevity

This section examines the reasons for consumption of inflatant, one of the two consumables in the SALTUS flight system, the other being propellant.^{2,3} Our discussion of how the total inflatant needs of *M1* are calculated is a bounding argument and not a precise inflatant usage calculation. The goal of our present argument is to show that the planned 200 kg reservoir of inflatant will last at least 5 years and maybe out to 10 years, not that it will be exhausted at a specific hour.

The four sources of inflatant loss are permeation through the membrane, effusion through MM-induced holes, venting of excess gas when moving from a cold attitude to a hot one, and valve and fitting losses. Each one is examined in turn, and at the end of this section, the lifetime is examined collectively under a variety of parameter arrangements to demonstrate the robustness of the longevity of the inflatant inventory.

3.4.1 Permeation of the membrane

The permeability of gases through polymeric material varies widely as a function of the permeant gas species, the membrane material, and especially temperature.^{44,45} Here, we consider the case of helium permeating through a polyimide membrane at 45 K, the “hot” end of the *M1* operating temperature range. Data on the permeability characteristics of noble gases through Kapton[®] film can be found in Schowalter et al.⁴⁵

The permeation rate is given as

$$Q = K \frac{A}{d} \Delta P, \quad (16)$$

where Q is the number flow rate, K is the permeability, A is the surface area, d is the membrane thickness, and ΔP is the pressure differential of the permeant gas across the membrane (here, simply the gas pressure within the reflector). The temperature dependence of the permeability is given as

$$K \propto \exp\left(-\frac{E_K}{k_B T}\right), \quad (17)$$

where E_K is the energy of permeation.

The permeability for helium determined by Schowalter et al.⁴⁵ for a temperature of 22°C is $K = 8 \times 10^{-10} \text{ cm}^3 \text{ @ STP mm} / (\text{Torrcm}^2\text{s})$.

For a pressure of 5.1 Pa, a membrane thickness of 12.7 μm , and a membrane area of 350.0 m^2 (corresponding to a physically inflated diameter of 15 m), the mass loss rate through both faces of the SALTUS *M1* would be $\sim 0.085 \text{ kg/year}$, or 85 g/year, at the assumed gas temperature of 45 K. It can be concluded that the gas loss via permeation is insignificant.

3.4.2 Micrometeoroid-induced losses

The holes created by MM impacts are an inevitable fact of life for gossamer systems such as *M1*. As a result, we must mitigate against the gas loss through a sufficiently large reservoir of replacement inflatant. To understand the problem, we first derive an expression of how *M1* will lose inflatant mass with time. With the initial result, we determine the pressure corrections needed to maintain *M1*'s shape (constant volume) over short and long time periods. Later in this section, we discuss the formation of penetration wounds in *M1* to determine the rate of increase in the hole area and its implications for inflatant loss over the mission lifetime.

Determination of effusion rate from M1. If a container of volume V has N molecules of molecular mass m inside it at temperature T , their velocities are given by the Maxwellian distribution. The average number of collisions J over an area A of gas against a container wall is found by integrating over the angle and velocity and is a classic textbook problem in the kinetic theory of gases.⁴⁶ J is given by

$$J = \frac{N}{4V} \sqrt{\frac{8k_B T}{\pi m}}. \quad (18)$$

The ideal gas law is

$$PV = nRT, \quad (19)$$

where n is the number of moles in the container and $n = N/N_A$, N_A is Avogadro's number, and P is the pressure. Solving Eq. (19) for N/V gives

$$\frac{N}{V} = \frac{PN_A}{RT}. \quad (20)$$

Substituting Eq. (19) into Eq. (18) gives

$$J = \frac{PN_A}{RT} \sqrt{\frac{k_B T}{2\pi m}}. \quad (21)$$

Equation (21) simplifies to

$$J = P \sqrt{\frac{N_A^2 k_B T}{2\pi m R^2 T^2}}. \quad (22)$$

Recalling that the universal gas constant R and the Boltzmann constant are related by Avogadro's number, $R = N_A k_B$ gives

$$J = P \sqrt{\frac{1}{2\pi m k_B T}}. \quad (23)$$

J is in collisions/area/time, so to get the rate of mass lost, $\dot{m} = (dm/dt)$, due to a hole of area A , J is multiplied by A , and the mass per molecule m results in

$$\dot{m} = JAm = -PA \sqrt{\frac{M}{2\pi N_A k_B T}}, \quad (24)$$

where A is the area of the hole, M is the molar mass, k_B is Boltzmann's constant, T is the temperature, and $m = M/N_A$. The total mass contained in M1 is described in terms of the moles, n , as

$$m = nM. \quad (25)$$

Substituting Eq. (25) into Eq. (24) gives

$$\dot{n}M = -PA \sqrt{\frac{M}{2\pi N k_B T}}. \quad (26)$$

Cancelling the factor of M in Eq. (27) and making the time derivative explicit result in

$$\frac{dn}{dt} = -PA \sqrt{\frac{1}{2\pi N k_B M T}}. \quad (27)$$

We know that the total area A of the holes caused by the MM environment is essentially a linear function of the elapsed mission time, S , so A is written as

$$A = \alpha S, \quad (28)$$

where A is the time-dependent area lost to penetrations and α is the area lost to MM impacts per time. Substituting Eq. (28) into Eq. (27) yields

$$\frac{dn}{dt} = -P\alpha S \sqrt{\frac{1}{2\pi N k_B M T}}. \quad (29)$$

Using the ideal gas law, we substitute for pressure in terms of the other gas variables, giving

$$\frac{dn}{dt} = -\frac{nRT\alpha S}{V} \sqrt{\frac{1}{2\pi N k_B M T}}. \quad (30)$$

Equation (30) simplifies to

$$\frac{dn}{dt} = -n \frac{R\alpha S}{V} \sqrt{\frac{T}{2\pi N k_B M}}. \quad (31)$$

It is important to note here that, for the timescale in which we are operating (the time between pressure corrections), there will be little change in S , V , and T . Therefore, although S , V , and T are functions of time in the long term, we treat them as constant for the purposes of solving Eq. (31) for the short time behavior. Equation (31) is a separable differential equation with constant coefficients, and its solution is

$$n(t) = n(0) e^{-t \frac{R\alpha S}{V} \sqrt{\frac{T}{2\pi N k_B M}}}. \quad (32)$$

The characteristic time τ of this exponential decay is

$$\tau = \frac{V}{R\alpha S} \sqrt{\frac{2\pi N k_B M}{T}}. \quad (33)$$

A key point in our analysis of Eq. (33) is the appearance of the $M1$ elapsed mission time, S , in the denominator. This means that the time to sense and correct any deficits in pressure becomes shorter as the mission goes on and more area is opened up. Equation (32) is rewritten using Eq. (33), resulting in

$$n(t) = n(0) e^{-\frac{t}{\tau}}. \quad (34)$$

A key operating parameter is the time for the gas to leak to the point at which P is out of tolerance, namely, $P(t) = P - \delta P$. To determine the time between injections of gas to maintain pressure, we write $\delta P(t)$ as

$$\delta P(t) = \frac{n(0)RT}{V} - \frac{n(t)RT}{V}. \quad (35)$$

Factoring out common terms and using Eq. (34) result in

$$\delta P(t) = \frac{n(0)RT}{V} \left(1 - e^{-\frac{t}{\tau}}\right). \quad (36)$$

Equation (36) is rewritten as

$$\delta P(t) = P(0) \left(1 - e^{-\frac{t}{\tau}}\right). \quad (37)$$

Solving Eq. (37) for t gives

$$t = \tau \ln \left(\frac{1}{1 - \frac{\delta P}{P(0)}} \right). \quad (38)$$

Substituting the definition of τ from Eq. (33) into Eq. (38) gives

$$t = \frac{V}{R\alpha S} \sqrt{\frac{2\pi N k_B M}{T}} \ln \left(\frac{1}{1 - \frac{\delta P}{P(0)}} \right). \quad (39)$$

With $\delta P \ll P$, Eq. (39) is linearized, resulting in

$$t = \frac{\sqrt{2\pi N k_B}}{R} \frac{1}{S} \frac{V}{\alpha} \sqrt{\frac{M}{T}} \frac{\delta P}{P(0)}. \quad (40)$$

The timescale for adding gas to $M1$ will be determined by design choices for mission lifetime (S), the geometric properties of $M1$ that define the volume, V , the environment that defines α , inflatant species (M), our pointing attitude (T), and error budget allocation ($\delta P/P_0$).

We now turn our attention to calculating the total gas needed over the mission lifetime, S . We previously defined the cumulative hole area due to impacts as a linear function of time, αS , which is written as

$$A(t) = A_{A1} t \int \phi(w) \pi \left(\frac{\kappa w}{2} \right)^2 dw, \quad (41)$$

where κ is a constant that relates the size of the hole to the size of the particle, A_{M1} is the surface area of $M1$, t is time, and the $\phi(w)$ represents a function describing the micrometeoroid flux as a function of size (diameter). Equation (41) assumes that the hole made in the membrane is circular. Equation (41) is rearranged to give

$$A(t) = t(A_{M1} \kappa^2) \frac{\pi}{4} \int \phi(w) w^2 dw. \quad (42)$$

In Eq. (42), the time dependence is the first term on the right side, the parenthetical term is the design-dependent term, and the area and the size of the damage hole (assumed constant with size and energy) are the numerical term and the integral term, respectively, and are dependent on the natural environment. Associating the constant term in Eq. (43) as α , we write the time rate of mass loss as

$$\frac{dm}{dt} = -t P (A_{A1} \kappa^2) \frac{\pi}{4} \sqrt{\frac{M}{2\pi N k_B T}} \int \phi(w) w^2 dw. \quad (43)$$

As complicated as Eq. (43) looks, it is very simple, that is

$$\frac{dm}{dt} = -t Q, \quad (44)$$

where Q is given as

$$Q = P (A_{A1} \kappa^2) \frac{\pi}{4} \sqrt{\frac{M}{2\pi N k_B T}} \int \phi(w) w^2 dw, \quad (45)$$

with a bounding lower value used for T . In Eq. (45), all of the terms except κ and $\int \phi(w) w^2 dw$ are known and constant. The impact of the collision, the magnification, and the wound caused by a particle of size d that enters Q as κ^2 are determined by hyper-velocity testing. The integral term is a property of the environment. The total inflatant mass needed is given by

$$m_{\text{gas}} = \int_0^S Q t dt, \quad (46)$$

which trivially integrates to

$$m_{\text{gas}} = \frac{Q}{2} S^2. \quad (47)$$

Equation (47) clearly shows that the inflatant gas mass is proportional to the square of the mission length, S^2 .

Area of $M1$ lost to micrometeoroid penetration. When an MM exceeds the ballistic limit and penetrates a membrane, such as $M1$, a wound results on both layers of the lenticular. As described previously, we seek a bounding analysis of inflatant consumption. The goal of this

section is the bounding analysis of the impactor wound area and its effects on inflatable consumption.

In the previous section, we showed that the mass loss rate depends on many variables; some, such as pressure, temperature, and gas species, are easy to comprehend. The total area of penetration or total wound area is much harder to grasp with simple physical intuition. The evolution of the wound area over mission life must be estimated conservatively to make a robust assessment of the lifetime of an inflatable system necessary for the viability of the SALTUS mission concept.

We recently reported on the propagation of MM in gossamer structures giving a predictive model of fragmentation.⁴⁷ An even more recent report gave a further experimental examination of fragmentation and penetrations of gossamer systems and provided further insight into this complex problem.⁴⁸

The impact of an MM on a series of gossamer layers is shown schematically in Fig. 28. The image shows the clean initial penetration and fragmentation of the impactor and the propagation of fragments creating exit wounds.

Figure 29 shows micrographs of recent hypervelocity tests and demonstrates the experimental evidence of fragmentation of a large impactor. The entrance wound is a clean circular wound, and the shock from the collision shatters the impactor into fragments that follow a power law distribution. Each of the fragments from the collision with the first surface shatters at the second

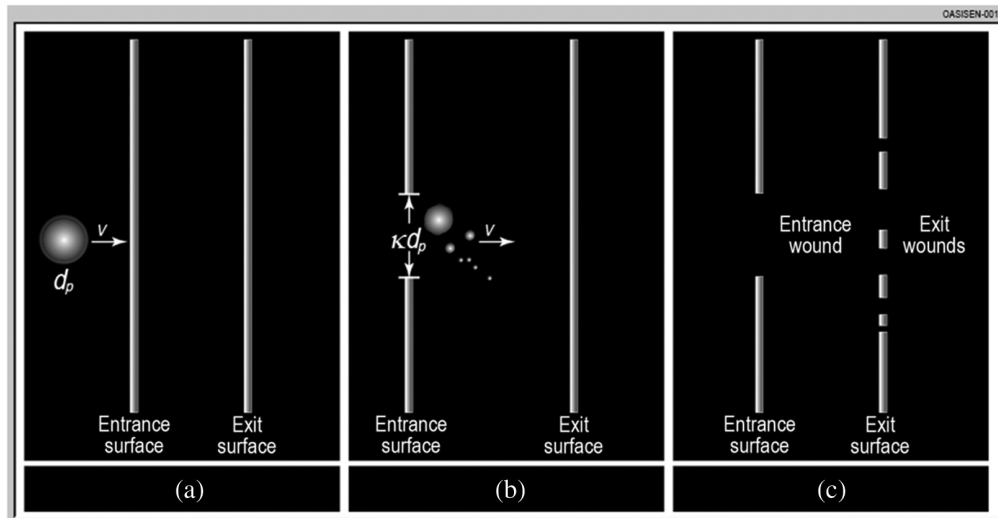


Fig. 28 Fragmentation on propagation in gossamer structures from Ref. 24. (a) Micrometeoroid of diameter d_0 incident (b) Entrance wound κd_0 diameter and initial impactor has fragmented (c) exit wounds left by fragments.

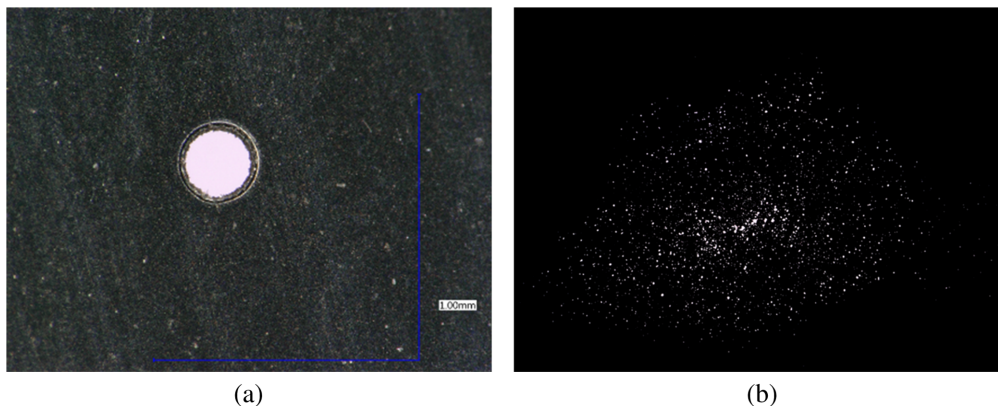


Fig. 29 Entrance and second layer damages from Ref. 40.

surface, each one into a power law, with the largest particle decreasing in size and the slope becoming steeper. This process of sequential fragmentation has been discussed recently.⁴⁷

The recent tests carried out involved many layers of different materials and impactor velocities to collect data for other goals and to further validate our recent propagation model. Examples of the typical results are shown in Figs. 30 and 31. Figure 30, which is a test of typical ½ mil thick polyimide layers, has the same material used for the development of the propagation model.⁴⁷

One of the materials recently tested and reported was a ½ mil thick layer of a composite nature, which is significantly more damage resistant, as shown in Fig. 31.⁴⁸ The distribution of fragments indicates a smaller maximum particle size and steeper slopes indicative of much less wound area on the membrane. This indicates that modern materials and proper selection can play a role in minimizing MM damage and increasing mission life.

One of the key results of our recent work⁴⁷ was the calculation of the specific area lost for various membrane thicknesses and numbers of layers for the entire flux of impactors. The estimate of the specific area loss rate in units of $\text{cm}^2/\text{m}^2/\text{year}$ denoted as Λ for the baseline ½ mil polyimide material is the basis of our damage area estimation.

Creep can affect the determination of the overall wound area. A simple model of this effect is an increase in wound area with time. Let us call the increase in area with time γ and furthermore assume that creep is constant in time.⁴⁹ The linear estimation of creep provides a clear upper limit to this effect as creep at a given load and temperature is explicitly a monotonically decreasing function of time. The resulting overestimation of the impact of creep also provides a clear

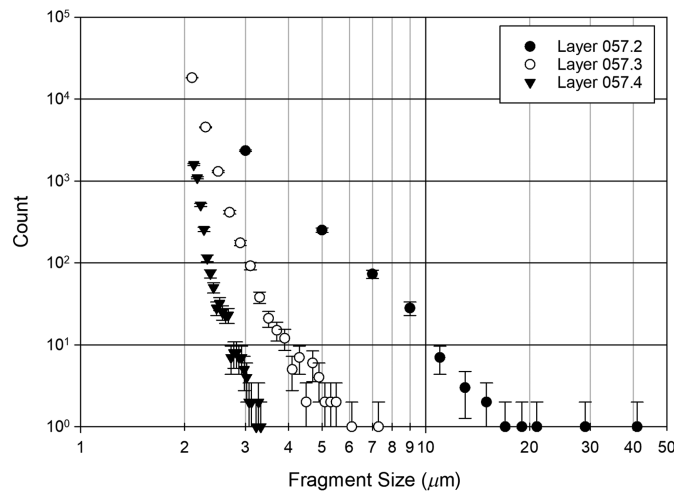


Fig. 30 ½ mil VDA.

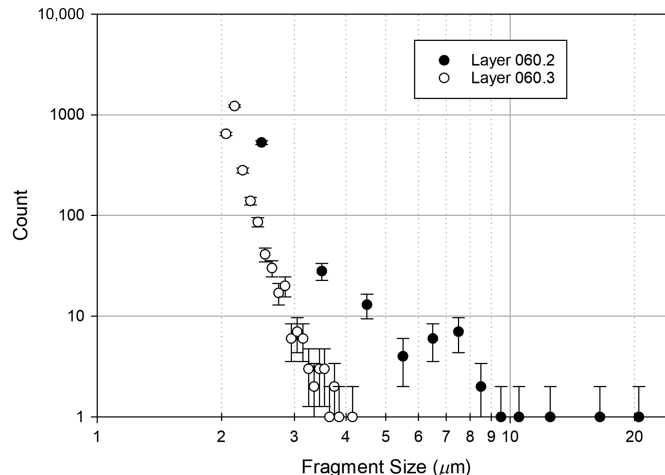


Fig. 31 ½ mil strengthened laminate.

bounding case. The linear approximation also makes the calculation easier to follow. Our simple (and bounding) model of the hole area at time interval k including creep is written as

$$A_k = a(1 + \gamma(k-1)) + a(1 + \gamma(k-2)) + \dots + a, \quad (48)$$

where A_k is the total area at the k 'th week and a is the area generated in a time interval. Equation (48) is more compactly written as

$$A_k = \sum_{j=0}^{k-1} a(1 + j\gamma). \quad (49)$$

Equation (49) expands to

$$A_k = ka + \gamma a \sum_{j=0}^{k-1} j \quad (50)$$

Using the well-known formula for the summation of an arithmetic series, Eq. (51) becomes

$$A_k = ak + \gamma \frac{k(a(k-1) + a)}{2}, \quad (51)$$

and with simplification, we arrive at

$$A_k = ak + \gamma a \frac{k^2}{2}. \quad (52)$$

The term a is the rate of increase in the hole area per time interval. For our current analysis, the time interval is a week and is written as

$$a = 2A_{M1} \frac{\Lambda}{52}, \quad (53)$$

where A_{M1} is the physical area of $M1$ and the factor of 2 is included as there are two membranes in $M1$. Substituting Eq. (53) into Eq. (52) gives

$$A_k = A_{M1} \frac{\Lambda}{26} \left(k + \gamma \frac{k^2}{2} \right). \quad (54)$$

The inclusion of the impact of creep [Eq. (54)] in the analysis that leads to Eq. (47) will introduce a term proportional to the cube of mission time, S .

At low temperatures of ~ 45 K, the maximum operating temperature for $M1$ creep is expected to be nil⁴⁹ and can be easily tested early in the program before making a choice of the flight membrane material.

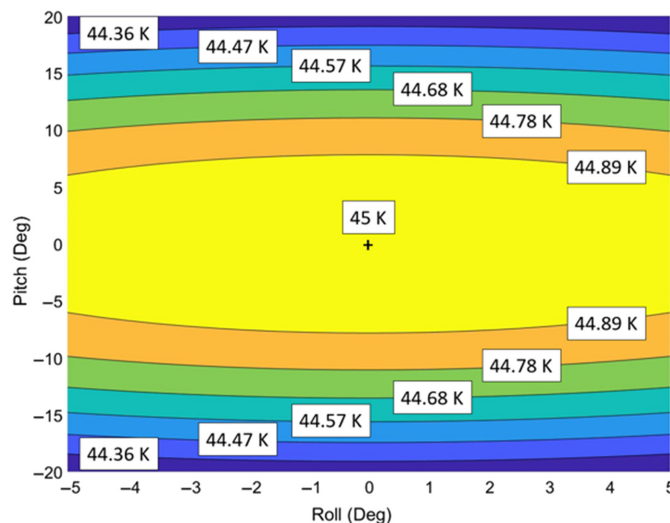


Fig. 32 Map of peak $M1$ temperature.

3.4.3 Cold to hot pointing losses

The temperature of $M1$ will change due to the differences in solar illumination as the spacecraft attitude changes over the FOR. As we want the shape of $M1$ to remain static, we need to design for adjustments in the gas during these events. We calculate the difference in moles of inflatant needed to maintain $M1$ at constant pressure and volume as the gas temperature changes from hot to cold, or vice versa. The ideal gas law under these conditions gives

$$nT = \frac{PV}{R}, \quad (55)$$

where n is the number of moles, T is the temperature, P is the pressure, V is the volume, and R is the gas constant. We then describe the change in our initial conditions to our final conditions as

$$n_i T_i = n_f T_f. \quad (56)$$

Rearranging Eq. (56) gives

$$n_f = \frac{n_i T_i}{T_f}. \quad (57)$$

We define n_f in terms of the adjustment or change in the number of moles needed as

$$n_f = n_i + \Delta n. \quad (58)$$

Substituting Eq. (58) into Eq. (57) gives

$$\frac{n_i T_i}{T_f} = n_i + \Delta n. \quad (59)$$

The solution of Eq. (59) results in

$$\Delta n = \frac{n_i T_i}{T_f} - n_i, \quad (60)$$

$$\Delta n = \frac{n_i T_i}{T_f} - \frac{n_i T_f}{T_f}, \quad (61)$$

and finally

$$\Delta n = \frac{n_i (T_i - T_f)}{T_f}. \quad (62)$$

From Eq. (62), we can see that, when SALTUS points from a cold to a hot attitude $T_f > T_i$, $\Delta n < 0$, and gas must be released from $M1$.

The flux and impact velocity of the MM will depend on $\cos \theta$, where θ is the angle between the surface element's normal and the sun vector. The sun vector in the body coordinate frame is given as

$$\hat{s} = \langle \cos \beta \cos \gamma, -\sin \gamma, \sin \beta \rangle \quad (63)$$

where β is the solar pitch and γ is the solar roll. We then calculate $\cos \theta$ using the dot product of the sun vector and sunshield normal, to give

$$\cos \theta = \hat{n} \cdot \hat{s} \quad (64)$$

and calculate the temperature of $M1$. Figure 32 gives a map of the $M1$ mean temperature as a function of pitch and roll.

Equation (62) shows that Δn is negative if $T_f > T_i$, a cold to hot pointing change. Figure 33 evaluates Eq. (62) over the full range of possible pointings (temperatures) given an initial pointing (temperature). The three initial pointing conditions are the three panels in Fig. 33: the coldest pointing, ± 20 deg pitch, ± 5 deg roll; an attitude near the middle of the FOR, $+15$ deg pitch, 0 deg roll; and the hottest pointing, 0 deg pitch, 0 deg roll. For the coldest pointing, the leftmost panel, every other pointing attitude requires venting of inflatant, a maximum of 0.025 moles.

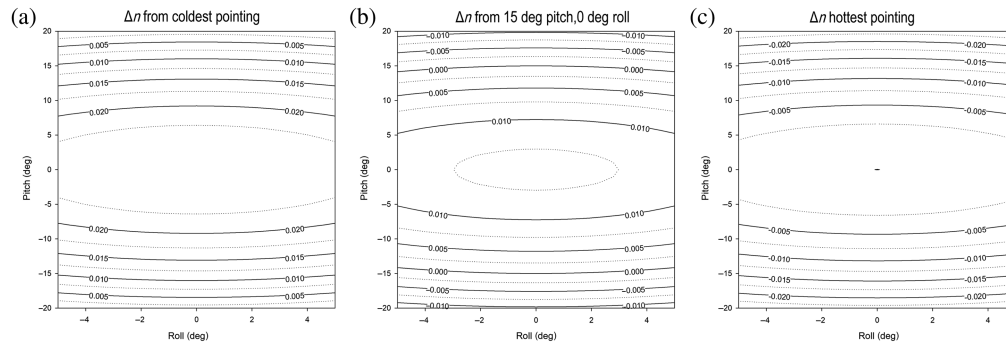


Fig. 33 Contour plots of inflatant that must be vented to reach P_0 when moving from the initial pointing to any other point in the FOR; the initial point in panel (a) is ± 20 deg pitch, ± 5 deg roll; in panel (b), $+15$ deg pitch, 0 deg roll; and in panel (c), 0 deg pitch, 0 deg roll.

For the middle pointing, a move to a lower pitch value requires venting, a maximum of ~ 0.017 moles, and moves to greater pitch angles require no venting. When the initial pointing is at the center of the FOR, the hottest point in the FOR, all other attitudes are cooler and require no venting upon repointing.

3.4.4 Valve losses

Valve losses, both internal and external, are given by the manufacturers and are standard measures of performance. For a conservative estimate, we assume that all valves leak for the entire mission, and we assume that the amount of mass loss is the sum of the internal and external leaks. This is truly conservative as the internal leak will end up in $M1$ and simply lower the amount of gas that the ICS injects. We, therefore, ignore this complication for this bounding estimate. The internal and external valve leak rates are taken from the manufacturer's catalog and are representative of this kind of hardware.

3.4.5 Inflatant lifetime net assessment

As described above, the net use of inflation comes from four main sources, each with their own complications. In this section, we report on the sum in a maximum use case, which in some sense is not completely physical or case consistent but is constructed to show that, even in this worst case, the inflatant will last 5 years and meet mission life requirements. Under more realistic conditions, the gaseous helium reserve will last all 10 years of the expected extended mission.

For the purposes of the current analysis, we define three cases: the least consumptive case (LCC), the current best estimate (CBE) (of conditions), and the most consumptive case (MCC). These cases will help bound inflatant usage and show that the baseline design will last at least the 5 years required under the most pessimistic case and is very likely to last all 10 years of the potential extended mission. The most optimistic conditions include easily imagined increased shielding, l included with the stiffening mesh in the truss, and protecting the back of $M1$. Our analysis shows how effective it might be, but this additional shielding is not part of the SALTUS design at the time of this writing. The LCC temperature of 25 K was chosen for its better sensitivity and impact on science, rather than for lifetime only. Later in this section, we relax that assumption; see Fig. 36. For conditions, we assume that SALTUS incurs maximal venting going from cold to hot attitudes. The rate of the venting is determined by the observation period for each set of conditions shown in Table 2. We assume that the attitude goes from hot to cold and then cold to hot, so this venting penalty is incurred every other observation, with the period determined by twice the observation length.

Figure 34 shows the amount of inflatant for the four consumptive terms under the MCC conditions. The largest consumption is from micrometeoroid holes, followed by the extra consumption caused by creep. As noted, before, at the operating temperatures, this is quite unphysical and is included to make a true MCC or worst-case analysis. The cold to hot venting and valve

Table 2 Definition of operating conditions, most optimistic, best estimate, and most consumptive.

	Least consumptive case (LCC)	Current best estimate (CBE)	Most consumptive case (MCC)
Temperature (K)	25	37	25
Λ [$\text{cm}^2/\text{m}^2/\text{year}$]	1.6×10^{-6}	1.6×10^{-6}	3.2×10^{-6}
Creep (/week)	10^{-6}	10^{-6}	0.001
Shielding	0.6	0.15	0
Mean observation length (h)	4	4	2

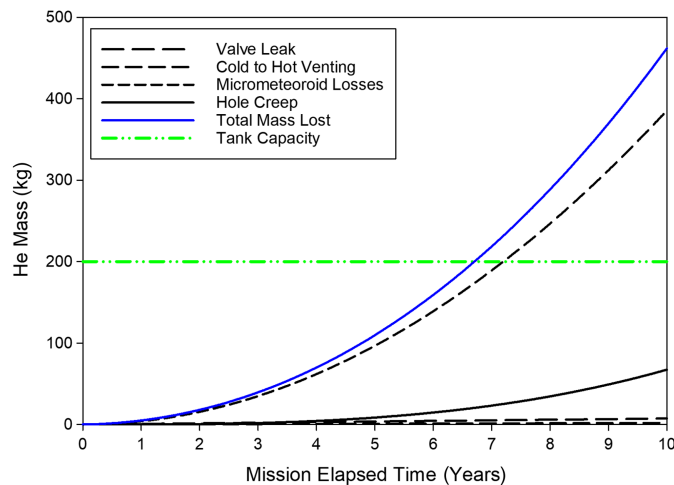


Fig. 34 Inflant consumption MEV.

losses are very small but visible. Figure 34 clearly shows that the inflatant will last 5 years and will be exhausted ~9 years, well past requirements.

Figure 35 shows the time-dependent usage of the inflatant in the CBE conditions. The order of consumption is the same, except for creep, which is effectively nil. Under this more realistic set of conditions, the inflatant will last all 10 years.

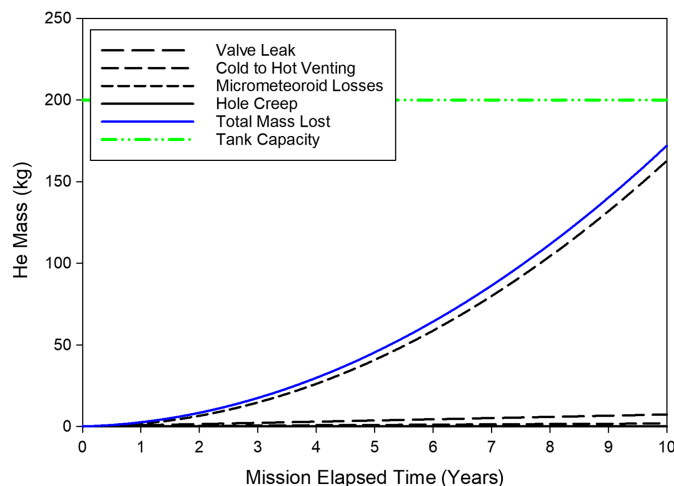


Fig. 35 Gas consumption CBE.

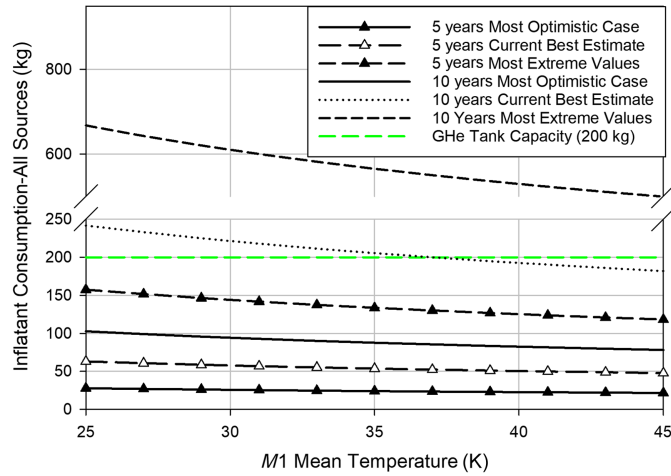


Fig. 36 Inflant requirements for LCC, CBE, and MCC cases over *M1* temperatures from 25 to 45 K.

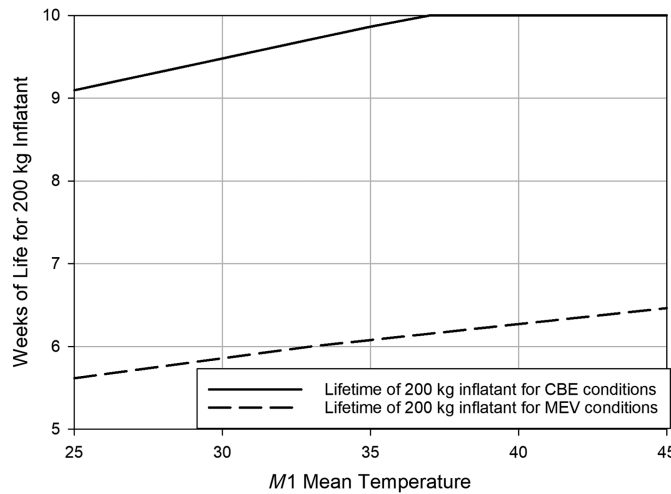


Fig. 37 GHe lifetime for CBE and MCC conditions over *M1* temperature from 25 to 45 K.

The readers can appreciate from our results that inflatant consumption is a complicated performance space depending on many parameters. To give the readers more insight, consider Figure 36, which shows the necessary amount of gas for the required 5-year mission and the possible extension to 10 years for the LCC, CBE, and MCC cases. One of the most influential variables in gas consumption is *T*. *T* is varied from 25 to 45 K, and it is clear from Fig. 36 that, in all cases, the minimum required lifetime of 5 years is met and exceeded.

To give further insight into the endurance of the inflatant inventory, the lifetime as a function of *M1* temperature was calculated. For LCC and all temperatures considered, the lifetime of the helium was longer than 10 years. The results for the CBE and MCC conditions were explicitly calculated and are plotted in Fig. 37. This figure clearly shows that, for any *M1* temperature, the minimum requirement of 5 years is met and that, under CBE conditions, the inflatant is likely to last at least 9 years, and for *T* > 37 K, a 10 year or slightly longer will result.

4 Planned Development Activities

Achieving TRL6 requires a demonstration of the performance of a relevant prototype in the proper environment. The chosen 8-m article is the relevant prototype as it allows us to complete the necessary testing before PDR as required within program funding and cost constraints. To achieve TRL6, we must demonstrate that *M1* can be constructed with the necessary precision,

Table 3 Tests on the SALTUS inflatable reflector articles.

Test	8M EDU	14M Qual	14M Flight
Surface measurement on support	Yes	Yes	Yes
Packaging and deployment without AstroMesh	Yes	Yes	Yes
Inflation	Yes	Yes	Yes
Ascent-vent	Yes, at flight condition	Yes, at flight condition	Yes, at flight condition
Thermal cycling	Yes	Yes	
Packaging and deployment under vacuum	Yes, at NASA Glenn NATF	No	No
Packaging and deployment	Yes	Yes	Yes
Random vibration	Yes	Yes, at qual level	Yes, at accep. level
Surface measurement	Yes	Yes	Yes

stowed, deployed, and inflated, and maintained in a relevant environment. Thus, a series of tests shown in Table 3 are planned to verify the design and inform subsequent development articles. The precision of the *M1*'s shape is determined by the tolerances on the cutting of the gores and their seaming and is proportional to the size. To demonstrate sufficient accuracy at the flight scale, the 8-m development article will have gore and seam tolerances 8/14 of the flight values and a similar optical prescription. When demonstrated, the results from the test of the 8-m article will show that an acceptable 14-m *M1* can be manufactured. The 8-m article will be installed in the 9-m “IRAD Reflector AstroMesh™,” a capital asset of Northrop Grumman, to demonstrate the ability to integrate, stow, deploy, and survive deployment environments at the reflector/truss level. These deployment tests will allow for multiple stow and deploy cycles and validate articulation margins and stowing procedures. Furthermore, a flight-like stow and environmental testing will show that we will not permanently crease *M1*. The deployment and inflation of the development *M1* will demonstrate the reflector to truss interface.

After testing at Northrop Grumman's Oxnard facility, the 8-m reflector (*M1* development article), the development ICS, and optical metrology equipment go to NASA's Neil Armstrong Test Facility (NATF) in Ohio. At NATF, the 8-m test article will be integrated into a ground support equipment support ring and inflated via the ICS (per Table 4) at atmospheric pressure and room temperature, to various pressures around the 5.1 Pa (gauge) and with several gases (gravity sag) and the shape measured. We will also tip the GSE interface ring at a few angles to provide a diversity of gravity environments. The 8-m reflector will then be placed in the environmental chamber—this is another reason to select the 8-m size as it will fit in the chamber. The air will be removed from the chamber in steps, allowing for shape measurements at various atmospheric pressures. After reaching the vacuum, the temperature will be lowered via the LN₂ shroud. A GSE heater plate will simulate the radiant load from the sunshield, and the heater plate will have several independent zones so that the gradient across the test reflector can be varied. Data from these tests will validate the thermal and distortion models. Each of these test conditions provides a unique test environment in terms of temperature, pressure, and gravity. Shape and other telemetry such as ICS sensor data will be compared with predictions and the shapes compared with an *a priori* established performance requirement. The data collected will also be used to update and validate the design models. At this point, *M1* will be at TRL6.

These experimentally validated design models, for gravity, temperature, and pressure and pressure control, will be used to design the 14-m *M1* units. *M1* will be measured in various stressing environments to show compliance with requirements in the test environments that are consistent with flight performance. At this point, *M1* is at TRL7.

Table 4 System development test objectives: test at NASA NATF with 8-m EDU M1.

Test objective	Test approach	Model validated	Use
Inflatable design process validation	Collect and trend optical metrology data of M1 from manufacture through the end of the test	Design codes (FAIM, FLATE) and flight FEM (system integrated model)	Design and on-orbit performance
Optical performance of M1 over temperature	Heater plates to adjust M1 temperature, vary inflation gases to validate gravity model of M1	System integrated model	Prediction of on-orbit performance
Demonstrate M1 shape over multiple inflation cycles	M1 shape data collected over periods of the ICS being active and then idle	Lifetime model of membrane behavior	Predicting and budgeting lifetime effects
Understand the impact of ambient pressure on M1 inflated shape	Collect M1 metrology at room temperature and press and vacuum and low temperature	Design codes (FAIM, FLATE) and flight FEM (system integrated model)	Allows shape verification to occur at ambient
Validate creep models	M1 metrology data over the test, including a high-temperature test	Lifetime model of membrane behavior	Predicting and budgeting lifetime effects
Inflation control system demonstration	Use EM of ICS to actively control pressure	ICS operating models	ICS system TRL maturity
Inflatable consumption	Measure leak rates, from fittings and deliberate holes	Inflatable consumption model	System lifetime prediction

The existence of the set of validated models for all relevant environments and environmental changes allows for the verification of the flight *M1* shape via measurements in a factory environment.

5 Summary

We have presented the mission-enabling element of SALTUS, namely, its large inflatable primary reflector, *M1*, and the reasoning behind our confidence in being able to realize this game-changing optic. We have reminded the reader that inflatable systems are not a novel idea. The novelty in *M1* is its accuracy, built on advances in manufacturing, and its longevity, estimated from extensive micrometeorite analysis and experiments. We have discussed the design process and solution to the problem of cutting and seaming two-dimensional gores to make an accurate near-parabolic shape. We have also given the analysis of how *M1* will function in its environment and how the design mitigates these responses. The sufficiency of the planned inflatable inventory has also been demonstrated to be robust, meeting the minimum 5-year mission under worst-case analysis. Finally, we give an overview of the specific development and testing planned for *M1* to deliver a high-performance primary for SALTUS.

Taken together, this is why the time is right to bring *M1* into operation, powering a revolution in far-IR science and living up to the promise of the mission's name. We and the rest of the SALTUS team are ready to make this great leap.

6 Disclosures

The authors declare no specific financial interests or other potential conflicts of interest with the work presented in this paper.

7 Code and Data Availability

Data sharing is not applicable to this article as no new data were created or analyzed.

Acknowledgments

The authors wish to acknowledge internal funding and support for this work as well as the rest of the SALTUS team. Funding for the authors from Northrop Grumman, L'Garde, and the University of Arizona was performed under respective internal funding. DA2 Ventures personnel was supported by funding from the University of Arizona.

References

1. G. Chin et al., "Single aperture large telescope for universe studies (SALTUS): science overview," *J. Astron. Telesc. Instrum. Syst.* **10**(4) (2024).
2. L. Harding et al., "SALTUS probe class space mission: observatory architecture & mission design," *J. Astron. Telesc. Instrum. Syst.* **10**(4) 042303 (2024).
3. J. W. Arenberg et al., "OASIS architecture: key features," *Proc. SPIE* **11820**, 118200S (2021).
4. Project Echo, <https://www.nasa.gov/centers/langley/about/project-echo.html> (accessed 5 April 2023).
5. C. H. M. Jenkins, Ed., *Gossamer Spacecraft: Membrane And Inflatable Structures Technology For Space Applications*, American Institute of Aeronautics and Astronautics, Inc. (2001).
6. J. M. Wilkes and D. K. Marker, "A review of membrane optics research," AFRL-DE-PS-TM-2005-1002. <https://apps.dtic.mil/sti/tr/pdf/ADA436429.pdf> (accessed 14 May 2024).
7. B. Authier and L. Hill, "Large inflatable parabolic reflectors in space," *Proc. SPIE* **0598** (1986).
8. I. Bekey, "Very large yet extremely lightweight space imaging systems," *Proc. SPIE* **4849** (2002).
9. A. B. Meinel and M. P. Meinel, "Inflatable membrane mirrors for optical passband imagery," *Opt. Eng.* **39**(2), 541–550 (2000).
10. Y. Takashima et al., "All reflective THz telescope design with an inflatable primary antenna for Orbiting Astronomical Satellite for Investigating Stellar Systems (OASIS) mission," *Proc. SPIE* **11820**, 118200P (2021).
11. G. T. Van Belle, A. B. Meinel, and M. P. Meinel, "The scaling relationship between telescope cost and aperture size for very large telescopes," *Proc. SPIE* **5489** (2004).
12. M. Soh, J. H. Lee, and S.-K. Youn, "An inflatable circular membrane mirror for space telescopes," *Proc. SPIE* **5638**, 262–271 (2005).

13. J. D. Moore et al., “Design and testing of a one-meter membrane mirror with active boundary control,” *Proc. SPIE* **5899**, 58990Z (2005).
14. R. Freeland and G. Veal, “Significance of the inflatable antenna experiment technology,” in *Proc. AIAA, AIAA-98-2104* (1998).
15. D. Kim et al., “14-m aperture deployable off-axis far-IR space telescope design for SALTUS observatory,” *J. Astron. Telesc. Instrum. Syst.* **10**(4) (2024).
16. A. L. Palisoc et al., “Analytical and finite element analysis tool for nonlinear membrane antenna modeling for astronomical applications,” *Proc. SPIE* **11820**, 118200U (2021).
17. H. Quach et al., “Deflectometry-based thermal vacuum testing for a pneumatic terahertz antenna,” *Proc. SPIE* **11820**, 118200W (2021).
18. C. K. Walker et al., “Orbiting astronomical satellite for investigating stellar systems (OASIS): following the water trail from the interstellar medium to oceans,” *Proc. SPIE* **11820**, 118200O (2021).
19. A. Palisoc et al., “Constructing highly accurate inflatable parabolic dish reflector antennas and solar concentrators,” in *AIAA SCITECH 2024 Forum*, January (2024).
20. M. W. Thomson, “The AstroMesh deployable reflector,” in *IEEE Antenn. and Propag. Soc. Int. Symp. 1999 Digest. Held in conjunction with: USNC/URSI National Radio Science Meeting (Cat. No.99CH37010)*, Orlando, FL, USA, Vol. **3**, pp. 1516–1519 (1999).
21. H. Choi et al., “Mid-to-high frequency characterization of inflatable membrane optics,” *Proc. SPIE* **11820**, 118200V (2021).
22. M. Bardi et al., “Effect of ionizing radiation on mechanical and thermal properties of low-density polyethylene containing pro-degradant agents,” in *Int. Nucl. Atlantic Conf.* (2009).
23. S. G. Prasad, A. De, and U. De, “Structural and optical investigations of radiation damage in transparent PET polymer films,” *Int. J. Spectrosc.* **2011**, 810936 (2011).
24. J. Arenberg et al., “Status of the JWST sunshield and spacecraft,” *Proc. SPIE* **9904**, 990405 (2016).
25. R. Kurland, *TRL-6 Report: Sunshield Membrane Materials and Coatings (D41171)*, Northrop Grumman (2006).
26. The thermo-formed doubly curved 0.5 mil thick Kapton membrane was funded by a L’Garde, IR&D project, 1998-2000.
27. G. Veal, “Highly accurate inflatable reflectors—phase II,” L’Garde Tech. Rep., LTR-86-GV-129 (1986).
28. A. L. Palisoc, “Large inflatable structures,” Final Rep. to the US Air Force, F29601-96-C-0131 (1999).
29. A. L. Palisoc, G. Williams, and D. Brandt, “Preliminary analysis document for the inflatable reflector development program (IRD),” L’Garde Tech. Rep., LTR-93-AP-023 (1993).
30. J. W. Arenberg, “Factors affecting the performance of an ultrastable telescope: turning over all the rocks,” *Proc. SPIE* **11115**, 111151B (2019).
31. NeXolve, “Low & zero CTE polyimides,” <https://nexolve.com/advanced-materials/low-zero-cte-polyimides/> (accessed 8 August 2024).
32. B. Y. Dharmadassa et al., “Formation of plastic creases in thin polyimide films,” *J. Appl. Mech.* **87**, 051009 (2020).
33. J. Fischer et al., “Cryogenic far-infrared laser absorptivity measurements of the Herschel Space Observatory telescope mirror coatings,” *Appl. Opt.* **43**, 3765–3771 (2004).
34. Northrop Grumman Interoffice Correspondence, “Contamination control plan compliance description for observatory integration and test,” JWST.2021.300.0007 (2021).
35. J. Arenberg, “Calculation of the effect of ice on the transmission of the James Webb Space Telescope,” *Proc. SPIE* **6692**, 66920S (2007).
36. J. W. Arenberg et al., “Determination of emissivities of key thermo-optical surfaces on the James Webb Space Telescope,” *Proc. SPIE* **9143**, 91433Q (2014).
37. J. Arenberg et al., “Radiance from an ice contaminated surface,” *Proc. SPIE* **9904**, 99046G (2016).
38. J. W. Arenberg et al., “Long term observations of molecular film accumulation (Conference Presentation),” *Proc. SPIE* **12224**, 122240R (2022).
39. <https://www.spennis.oma.be/>
40. E. Grün et al., “Collisional balance of the meteoritic complex,” *Icarus* **62**, 244–272 (1985).
41. J. I. Thorpe et al., “Micrometeoroid events in LISA pathfinder,” *ApJ* **883**, 53 (2019).
42. S. G. Love and J. H. Allton, “Micrometeoroid impact crater statistics at the boundary of earth’s gravitational sphere of influence,” *Icarus* **184**, 302–307 (2006).
43. R. L. Perry, III, “A numerical evaluation of the correlation of surface cleanliness level and percent area coverage,” *Proc. SPIE* **6291**, 62910L (2006).
44. D. J. Lovinger and R. B. Hallock, “Temperature dependence of helium diffusion through common epoxies,” *J. Phys.: Conf. Ser.* **400**, 052006 (2012).
45. S. J. Schowalter, C. B. Connelly, and J. M. Doyle, “Permeability of noble gases through Kapton, butyl, nylon, and ‘Silver Shield’,” *Nucl. Instrum. Methods Phys. Res. A* **615**, 267–271 (2010).
46. R. L. Liboff, *Kinetic Theory*, Prentice-Hall, Englewood Cliffs, New Jersey (1990).

47. M. N. Villarreal, J. W. Arenberg, and L. H. Harris, "Predictive model for micrometeoroid damage to gossamer structures," *J. Astron. Telesc. Instrum. Syst.* **8**(4), 044006 (2022).
48. L. Coyle et al., "ULTRA final report," https://nspires.nasaprs.com/external/viewrepositorydocument/cmdocumentid=984808/solicitationId=%7B7FF7A769-0D6A-AED7-1B6A-FE12CE6F7847%7D/viewSolicitationDocument=1/D.19%20ULTRA-TM_Final_Report.pdf (accessed 7 May 2024).
49. A. Antimov et al., "Large-area Kapton x-ray windows," *Proc. SPIE* **9588**, 95880F (2015).

Jonathan W. Arenberg is currently the chief mission architect for Science and Robotic Exploration at Northrop Grumman. His work experience includes the Chandra X-ray Observatory, co-invention of the starshade, and the James Webb Space Telescope. He is the chief architect and project systems engineer for SALTUS. He is an associate fellow of the AIAA and a fellow of SPIE.

Leon K. Harding is a senior staff engineer at Northrop Grumman. He received his PhD in astrophysics from the University of Galway in Ireland. Before Northrop Grumman, he held a research associate professorship at the Virginia Tech National Security Institute and was the assistant director of the Mission Systems Division. He was a technologist at the Jet Propulsion Laboratory and a scientist at Caltech. He is the spacecraft lead and deputy chief observatory architect for SALTUS.

Bob Chang is currently in the business development team of the Northrop Grumman Deployables Operating unit, which is responsible for large space deployables, such as booms and AstroMesh™ reflector assemblies. Prior to this current role, he spent 10 years as a mechanisms engineer with contributions to various programs, such as GOES, Osiris-REX, SWOT, Parker Solar Probe, Bepi Colombo, and JUICE.

Steve Kuehn has been a structural analyst at NGAS Deployables, formerly Astro Aerospace, since 1989. Starting in 1995, he has been involved in the development of the AstroMesh™ reflectors and several AstroMesh™ flight programs. He obtained his BS degree in mechanical engineering from California Polytechnic State University and his MS degree in mechanical engineering from Stanford University.

Dave Oberg is a program manager with Northrop Grumman, in the Science and Robotic Exploration unit. In this position, he works with scientists on initial concept development and then leads the team through design, production, and launch. He obtained his bachelor's and master's degrees in aeronautics and astronautics from the Massachusetts Institute of Technology.

Michaela N. Villarreal is a physicist at Northrop Grumman currently working on navigation systems and sensors and was previously a systems engineer as part of their Science and Robotic Missions group. She received her bachelor's degree in planetary science from UC Berkeley and her MS degree and PhD from UCLA in geophysics and space physics. She was previously a science team affiliate of NASA's Dawn and Europa Clipper missions.

Arthur L. Palisoc is currently the chief technology officer at L'Garde, Inc. His work experience includes the design and testing of the surface accuracy measurement system for the 14-m diameter inflatable antenna experiment reflector flown in 1996 on board the STS-77 Space Shuttle mission. He co-developed FAIM, the finite element analyzer code for inflatable membranes, which is used extensively in the characterization of the geometric nonlinear behavior of membrane shapes under load.

Christopher K. Walker is a professor of Astronomy, Optical Sciences, Electrical & Computer Engineering, Aerospace & Mechanical Engineering, and Applied Mathematics at the University of Arizona since 1999. He has worked at TRW and the Jet Propulsion Laboratory and was a Millikan Fellow in physics at Caltech. He has led numerous NASA and NSF projects, authored/coauthored 130+ papers, and published two textbooks: "Terahertz Astronomy" and "Investigating Life in the Universe."

Daewook Kim is an associate professor of Optical Sciences and Astronomy at the University of Arizona. He has devoted his efforts to a multitude of space and ground-based large optical engineering projects over a broad range of wavelengths, ranging from radio to x-ray. He has written

more than 300 journal/conference papers and is an associate editor for Optics Express. He is an SPIE fellow and was elected to the SPIE board of directors for the term 2024–2026.

Zach Lung is a space program strategist, business development manager, and scheduling lead at DA2 Ventures. He received his BS degree in business from Colorado State University in 2016. His professional background includes mission planning, proposal management, and technical writing for astrophysics, heliophysics, and ground-based astronomy observatories, including work on the Giant Magellan Telescope (GMT) as part of the US Extremely Large Telescope Program (US-ELTP).

Dave Lung has over 40 years of aerospace industry experience in a wide variety of air and space technologies and systems. He is currently the founder/president of DA2 Ventures, a consulting firm specializing in tech transfer, program planning, capture management, and proposal management. His education includes BS Aerospace Engineering, University of Minnesota (1985), MS Reliability Engineering, University of Arizona (1987), MBA University of Texas (1988), and post-graduate studies in Systems Engineering (USAF-AFIT). He was an officer in the USAF from 1984–1992.